Singularity Analysis and Steering Control Laws for Adaptive-skew Pyramid-type Control Moment Gyros

Hirohisa Kojima[a,*]

[a] *Tokyo Metropolitan University, Department of Aerospace Engineering, 6-6 Asahigaoka, Hino, Tokyo 191-0065, Japan*

Abstract

In contrast to past studies that have treated the skew angle as fixed in pyramid-type control moment gyro (CMG) systems, this paper treats the adaptive-skew pyramid-type CMG (ASCMG) system, in which the skew angle is one of the control variables for generating torques. The singular surfaces of the fixed-skew CMG are analyzed and visualized to illustrate how they depend on the skew angle, and the singular surfaces of the ASCMGs are also analyzed and visualized from a viewpoint of null motion for not only the gimbal angle but also the skew angle. The steering control laws are presented, and we numerically study their effectiveness for the reduction of settling time as compared to the fixed-skew pyramid-type CMGs.

Keywords: Control moment gyros; Singularities; Skew angle; Attitude maneuver

Nomenclature

$\boldsymbol{C}$	=	Jacobian matrix of the fixed-skew CMGs system
$\boldsymbol{D}$	=	Jacobian vector of the ASCMGs system associated with the skew angle
$\boldsymbol{g}_i$	=	the i^{th} gimbal axis vector
H	=	angular momentum magnitude of each CMG (= 0.0419 Nms)
$\boldsymbol{h}$	=	angular momentum vector of the CMGs
$\boldsymbol{h}_s$	=	singular momentum vector of the CMGs
$\boldsymbol{H}_i$	=	angular momentum vector of the i^{th} CMG
$\boldsymbol{H}_s$	=	angular momentum vector of the spacecraft

*Corresponding author
Email address: hkojima@sd.tmu.ac.jp, tel: +81-42-585-8653, fax: +81-42-583-5119 (Hirohisa Kojima)

$\boldsymbol{I}_i$ = identity matrix with dimension of i

$\boldsymbol{J}$ = moment of inertia tensor of the spacecraft, kgm^2

$\boldsymbol{u}_s$ = singular vector

$\boldsymbol{Q}$ = Jacobian matrix of the ASCMGs system = $[\boldsymbol{C}, \boldsymbol{D}]$

β = skew angle, rad

$\boldsymbol{\delta}$ = gimbal angle vector (= $(\delta_1, \delta_2, \delta_3, \delta_4)^T$)

δ_i = gimbal angle of the i^{th} CMG, rad

δ_{si} = singular gimbal angle of the i^{th} CMG

ε_i = the i^{th} signum of the singular surface

$\boldsymbol{\omega}$ = angular velocity of the spacecraft, rad/s

1. Introduction

Control moment gyros (CMGs) are momentum-exchange torque generators. These systems have the advantages of high torque output and rapid response compared to reaction wheels (RWs). CMG systems can be classified into two types based on the degrees of freedom for each CMG: single-gimbal CMGs (SGCMGs) and double-gimbal CMGs (DGCMGs). DGCMGs are mechanically more complex than SGCMGs, but the additional gimbal can be used to produce torque more easily. SGCMGs systems are mechanically simpler than DGCMGs, but in order to produce torque along an arbitrary direction, at least three SGCMGs are required.

There are many kinds of CMG array configurations, such as skew type, roof type, symmetric type, and twin type. The pyramid-array CMG system (Fig. 1) is one of the typical configurations for SGCMGs. Even though more than three SGCMGs are used, SGCMG systems have a more critical singularity problem than do DGCMG systems. The angular momentum of a pyramid-array CMG system in the singularity state was studied in [1].

To overcome the singularity problem of SGCMGs, a number of control schemes have been proposed[2]-[29]. From the viewpoint of basic control strategy, the control logic for singularity avoidance can generally be classified into two categories: gimbal path planning using offline calculation and real-time feedback control. Offline calculation methods search gimbal path trajectories so that the CMG systems do not

encounter any singularities. For such methods, workspace restrictions [3], preferred gimbal angles [4], and path planning [5] have been proposed. These methods have advantages in global singularity avoidance, and the optimal solution for gimbal planning was obtained using the pseudospectral method[6]. However, these methods typically have a high computational cost; thus, they are not suitable for real-time implementation.

On the other hand, the real-time CMG steering methods are simpler than the offline calculations, but special techniques are required to avoid singularities. Real-time singularity avoidance methods can be classified into four types: singularity-robust (SR) inverse steering laws[7, 8, 9, 10, 11], the singular direction avoidance (SDA) method [12], the gradient method[7, 21, 22, 23, 24, 25], and variable-speed CMGs (VSCMGs)[22, 23, 24, 25, 26].

The SR method was originally proposed for the inverse kinematics solution of robot manipulator control problems[30] and then was applied to CMG steering control problems[7]. SR steering laws attempt singularity avoidance by adding torque error near the singularities, but this is not always successful. To overcome this problem, a generalized SR steering law[10] was proposed, in which an off-diagonal matrix with time-dependent modulation is used. In the gradient method, additional null motions are used for singularity avoidance[7, 21, 22, 23, 24, 25]. VSCMGs avoid singularities by changing the wheel speed. In this sense, VSCMGs have functions of both CMGs and RWs. The control methods cited above (singularity-robust, singular direction avoidance, gradient, and variable-speed) are combined to increase the effectiveness of CMG systems. Leve and Fitz-Coy have proposed other metric that depends on the type of singularity (hyperbolic or elliptic), and the hybrid steering logic that combines the local gradient (LG) term and singular direction avoidance (SDA) term in which the weighting coefficients for the two terms vary in accordance with the metric[21].

Because the singular surfaces can be obtained in advance, Kurokawa proposed a concept of global singularity avoidance based on planning an angular momentum path that avoids predetermined singular surfaces[20]. Takada and Kojima have implemented receding-horizon (RH) control for the CMG steering law[27] and also implemented the concept of Ref.[20] using the surface cost function as a singularity metric[28].

In ordinary pyramid-array systems, the skew angle is fixed at $\beta = \tan^{-1}\sqrt{2}$ rad ($= 54.73$ deg) because,

in this case, the shape of the momentum envelope approaches a sphere, and the system can easily cover an arbitrary direction. In other words, the areas covered by the momentum envelope depend on the skew angle, and thus the maneuver settling time depends on the skew angle. In contrast to these pyramid-type CMGs systems that were described in past studies, the adaptive-skew CMG (ASCMGs)[29] is considered in this paper. In the ASCMGs, the skew angle is treated as a variable to increase the angular momentum in the desired direction. To this end, a mechanism for changing the skew angle is designed and developed. The singular surfaces, which correspond to skew angles other than the traditional fixed skew angle (54.73 deg), are analyzed and visualized to illustrate how they depend on the skew angle.

In [29], in order to shorten the maneuver settling time, the skew angle was changed before starting an attitude maneuver in accordance with the maneuver axis. In contrast to the previous study, in this study the skew angle is assumed to be controlled during a maneuver. To consider such a situation, the singular surfaces of the ASCMGs are analyzed from a viewpoint with respect to the freedom of the skew angle number to change. Our analysis shows that the momentum envelope of the ASCMGs associated with the change of the skew angle, envelopes the momentum envelope of the fixed-skew CMG, and that despite the skew angle's freedom to change, there still exist internal singularities, some parts of which are identical to the internal singularities of 2-SPEED CMG[31], but others are different from that of both the traditional CMGs and 2-SPEED CMG because of the skew angle's freedom to change.

Two steering control laws, which treat the skew angle as one of the controllable variables, are presented by referring to the existing steering law for the fixed-skew CMGs. Results of numerical simulations will be presented to demonstrate the effectiveness of the ASCMGs for fast attitude maneuver, compared to the fixed-skew CMGs.

2. Adaptive-skew CMGs

2.1. Conceptual Position of ASCMGs

In contrast to traditional pyramid-mounted single-gimbal CMGs, the ASCMG system treats the skew angle as one of the available gimbals. Based on the type of gimbals for each CMG, the proposed adaptive-skew pyramid-array CMG system can be classified as either a single- or double-gimbal CMG. However, the skew angle of each CMG cannot be changed independently. For this reason, the ASCMG system

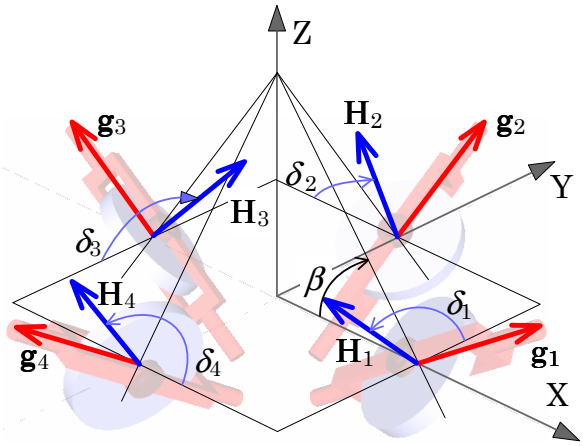

Figure 1: Pyramid-type CMG.

can be conceptually considered as an intermediate system between single- and double-gimbal CMGs, as shown in Fig. 2.

Note that we assume $0 < \beta \leq \pi/2$ rad in this paper because the CMG system becomes a system of four parallel single-gimbal CMGs when $\beta = 0$ rad, and in such a case, the rank of the CMG Jacobian is always less than three, and the CMG system cannot generate torque in arbitrary directions. Besides, the CMG system becomes a 2-SPEED system[31] when $\beta = \pi/2$ rad (= 90 deg), and in this paper, some analytical results are explained based on the 2-SPEED system configuration.

For the numerical simulations that will be shown later, we assume that the available range of the skew angle is $\pi/18$ rad (= 10 deg) $\leq \beta \leq 80\pi/180$ rad (= 80 deg) because the skew angle can only be between 10 and 80 deg due to the mechanical limitations of the experimental setup that we have developed.

Provided that the magnitude of the angular momentum for each CMG unit is unity, the maximum angular momentum along the x- or y-axis is given by $2 + 2\cos\beta$, and the maximum angular momentum in the z-axis direction is given by $4\sin\beta$. Using these equations, the maximum angular momentum along each axis for each skew angle can be summarized as shown in Table 1. The maximum angular momentum along the z-axis for $\beta = 80\pi/180$ rad (= 80 deg) is about 1.25 times that for $\beta = \tan^{-1}\sqrt{2}$ rad (= 54.73 deg), and the maximum angular momentum along the x- or y-axis for $\beta = \pi/180$ rad (= 10 deg) is about 1.26 times that for $\beta = \tan^{-1}\sqrt{2}$ rad (= 54.73 deg). Therefore, it can be expected that the available

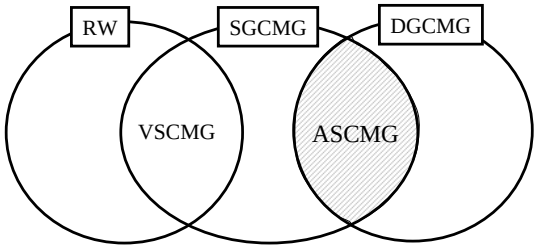

Figure 2: Conceptual classification of adaptive-skew pyramid-type CMGs.

maximum control torque around the z-axis would become larger, and the settling time for maneuvering around the z-axis would be reduced. Similarly, because the maximum available control torque around the x- or y-axis is increased, whereas the control torque around the z-axis becomes low when the skew angle is reduced, the settling time for maneuvers around the x- or y-axis would be reduced.

Table 1: Maximum angular momentum along each axis for each skew angle.

Axis	$\beta = 10$ deg	$\beta = 54.73$ deg	$\beta = 80$ deg
x, y	3.94	3.15	2.35
z	0.695	3.27	3.94

The volumetric relationship among the momentum envelopes of the fixed-skew CMGs, ASCMGs, and four DGCMGs can be represented as

$$\text{SGCMGs} \subset \text{ASCMGs} \subset \text{DGCMGs}. \tag{1}$$

Although the maximum momentum of the ASCMGs in the gimbal axis direction of the traditional fixed-skew CMG is almost the same as that of the traditional fixed-skew CMG, for the case that the skew angle can be changed from 0 to $\pi/2$ rad, the maximum momenta of the ASCMGs in the x, y, and z directions are the same as those of the DGCMG. From this viewpoint, the ASCMG system will have the advantage in an attitude maneuver around the x-, y-, and z-axes over the traditional fixed-skew pyramid CMG. This prediction will be verified through numerical simulations.

2.2. Experimental module of ASCMGs

A mechanism is necessary for the ASCMGs to change the skew angle. In the ASCMGs, it is assumed that the four skew angles are not independently changeable among the four CMG units, but are controlled, keeping identical angles among the four CMG units. To realize this, it might be expected that a complicated mechanism is necessary. However, one degree of freedom is associated with the skew angle. This implies that only one actuator is necessary to change the skew angle. In fact, by adding only a gear to each CMG unit and one actuator for controlling the gears of the traditional pyramid-type CMG configuration, we succeeded in developing an experimental setup of the ASCMG system.

Figures 3(a) and (b) show the experimental apparatus of the ASCMGs and a mechanism to change the skew angle, respectively. Each CMG wheel is rotated by a brushless DC motor, and each gimbal is steered by a stepper motor. Each CMG unit has a controller that controls these motors independently. Each CMG has 1/4 round gears connected with one worm gear, as shown in Fig. 3(b). Figure 3(c) shows a magnification of the part around the worm gear. A stepper motor is located on the top of the center podium. This stepper motor drives and controls the skew angle of the CMGs by rotating the worm gear. This new ASCMG module is about 50 cm cubed in size, and 7 kg in weight. This weight is slightly heavier than the previous fixed-skew CMG module developed in our laboratory, due to the mechanism of controlling the skew angle. The module was installed on a spacecraft model. Spacecraft motion was demonstrated using a spherical air bearing whose rotational center was almost coincident with the center of gravity of the spacecraft model.

3. ASCMGs Singularities

In this section, we will first analyze the dependency of the singularities of a fixed-skew pyramid-type CMG on the skew angle. Then, we will study the singularities of the ASCMGs by taking into consideration the freedom of the skew angle to change.

3.1. Dependency of Fixed-skew CMG Singularities on Skew Angle

When the skew angle is changed in advance to the attitude maneuver, or it is controlled slowly, the ASCMG system is practically the same as the traditional fixed-skew CMG system. However, it is still

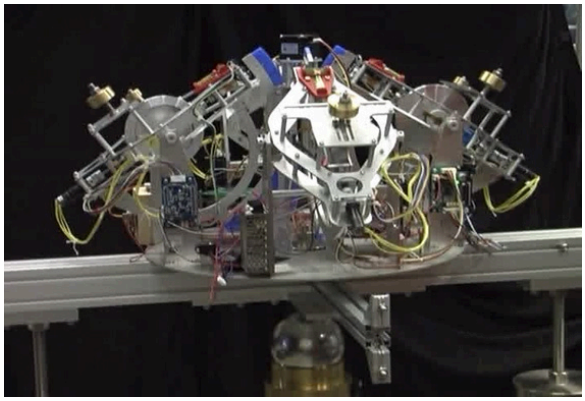

(a) ASCMGs module

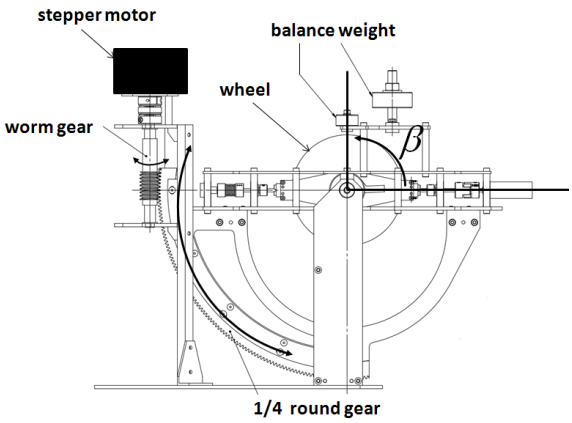

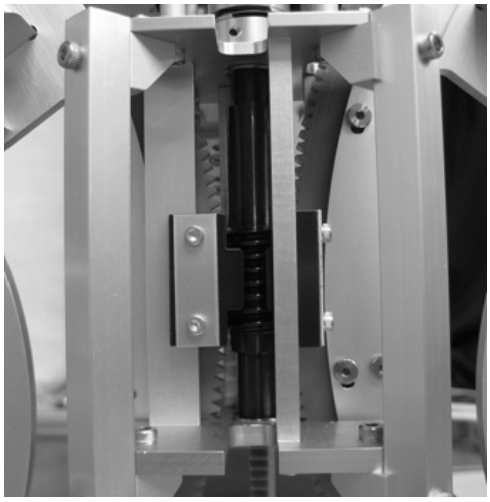

(b) mechanism to change the skew angle, and (c) magnification of the part around the worm gear.

Figure 3: The experimental apparatus.

desirable to study the dependency of the singularities of the CMG on the skew angle because such a study will give us an insight for designing a steering logic for the ASCMGs with respect to the skew angle.

For the pyramid mounting of four SGCMGs, the total CMG angular momentum vector $\boldsymbol{h}$ is expressed in the spacecraft reference frame as

$$\boldsymbol{h} = \sum_{i=1}^{4} \boldsymbol{H}_i = \begin{bmatrix} -c\beta \sin\delta_1 \\ \cos\delta_1 \\ s\beta \sin\delta_1 \end{bmatrix} + \begin{bmatrix} -\cos\delta_2 \\ -c\beta \sin\delta_2 \\ s\beta \sin\delta_2 \end{bmatrix} + \begin{bmatrix} c\beta \sin\delta_3 \\ -\cos\delta_3 \\ s\beta \sin\delta_3 \end{bmatrix} + \begin{bmatrix} \cos\delta_4 \\ c\beta \sin\delta_4 \\ s\beta \sin\delta_4 \end{bmatrix} \tag{2}$$

where $c\beta = \cos\beta$, $s\beta = \sin\beta$, and the momentum magnitude for each CMG is assumed to be a constant of magnitude one without loss of generality. In a traditional pyramid-array CMG system, the skew angle β is fixed to $\beta = \tan^{-1}\sqrt{2}$ rad (= 54.73 deg) because for this angle, the momentum envelope, which represents the maximum available angular momentum of the CMG for attitude maneuver, becomes nearly spherical.

The time derivative of the angular momentum vector for the fixed-skew CMGs can be obtained as

$$\dot{\boldsymbol{h}} = \sum_{i=1}^{4} \frac{\partial \boldsymbol{H}_i}{\partial \delta_i} \dot{\delta}_i = \boldsymbol{C}\dot{\boldsymbol{\delta}} \tag{3}$$

where

$$\boldsymbol{C} = \begin{bmatrix} -c\beta \cos\delta_1 & \sin\delta_2 & c\beta \cos\delta_3 & -\sin\delta_4 \\ -\sin\delta_1 & -c\beta \cos\delta_2 & \sin\delta_3 & c\beta \cos\delta_4 \\ s\beta \cos\delta_1 & s\beta \cos\delta_2 & s\beta \cos\delta_3 & s\beta \cos\delta_4 \end{bmatrix} \tag{4}$$

When $\dot{\boldsymbol{h}}$ from Eq. (3) lies in a plane for any choice of $\dot{\boldsymbol{\delta}}$, the CMG array cannot produce torque along the direction of vector $\boldsymbol{u}$ perpendicular to the plane of $\dot{\boldsymbol{h}}$, regardless of the gimbal rate. This situation is called a singularity. The corresponding gimbal angles are called the singular gimbal angles, the corresponding momentum vector is called the singular momentum vector, and the corresponding vector $\boldsymbol{u}$ is the singular vector. Because the torques generated by CMGs are always orthogonal to the gimbal axis vector, the

singular momentum vector $\boldsymbol{h}_s$ is expressed using the gimbal axis vector $\boldsymbol{g}_i$ and the unit vector $\boldsymbol{u}_s$ as

$$\boldsymbol{h}_s = \sum_{i=1}^{4} \frac{\varepsilon_i \left(\boldsymbol{g}_i \times \boldsymbol{u}_s\right) \times \boldsymbol{g}_i}{\left|\boldsymbol{g}_i \times \boldsymbol{u}_s\right|} \tag{5}$$

where $\varepsilon_i = \text{sign}\left(\boldsymbol{H}_i \cdot \boldsymbol{u}_s\right) = \pm 1$. When $\varepsilon_i = 1$, the resulting singular surface is the 4H singularity.

Let the singular vector $\boldsymbol{u}_s = (u_x, u_y, u_z)^T$ be expressed by a unit vector in polar coordinates as

$$\boldsymbol{u}_s = (\cos\theta_1 \cos\theta_2, \sin\theta_1 \cos\theta_2, \sin\theta_2)^T.$$

Taking into consideration the gimbal axis vectors for the pyramid-type CMGs with skew angle of β and a singular vector, and using Eq. (5), an analytical expression of the singular surfaces, $\boldsymbol{h}_s = (H_x, H_y, H_z)^T$, can be expressed as[32]

$$H_x = \frac{c\beta(-s\beta u_z + c\beta u_x)}{e_1} + \frac{u_x}{e_2} + \frac{c\beta(s\beta u_z + c\beta u_x)}{e_3} + \frac{u_x}{e_4} \tag{6}$$

$$H_y = \frac{u_y}{e_1} + \frac{c\beta(-s\beta u_z + c\beta u_y)}{e_2} + \frac{u_y}{e_3} + \frac{c\beta(s\beta u_z + c\beta u_y)}{e_4} \tag{7}$$

$$H_z = \frac{s\beta(-c\beta u_x + s\beta u_z)}{e_1} + \frac{s\beta(s\beta u_z - c\beta u_y)}{e_2} + \frac{s\beta(s\beta u_z + c\beta u_x)}{e_3} + \frac{s\beta(s\beta u_z + c\beta u_y)}{e_4} \tag{8}$$

where

$$e_1 = \pm\sqrt{1 - (s\beta u_x + c\beta u_z)^2} \tag{9}$$

$$e_2 = \pm\sqrt{1 - (s\beta u_y + c\beta u_z)^2} \tag{10}$$

$$e_3 = \pm\sqrt{1 - (-s\beta u_x + c\beta u_z)^2} \tag{11}$$

$$e_4 = \pm\sqrt{1 - (-s\beta u_y + c\beta u_z)^2} \tag{12}$$

3.1.1. Passable and Impassable Singularities for Fixed-skew CMGs[13]

The null motions of CMGs are defined as gimbal motions that generate no torque. These motions can be used to avoid or escape from CMG singularities, of which there are two kinds: hyperbolic and elliptic.

The hyperbolic singularities can be avoided through null motion, while the elliptic singularities cannot. In this section, we will briefly explain how to test whether null motion is possible at a given singularity and how to determine the type of singularity for a pyramid-type CMG with a fixed skew angle.

The condition for null motion of a pyramid-type CMG can be expressed using a Taylor series as follows:

$$\delta \boldsymbol{h} = \sum_{i=1}^{4} \left[\frac{\partial \boldsymbol{H}_i}{\partial \delta_i} \Delta\delta_i + \frac{1}{2} \frac{\partial^2 \boldsymbol{H}_i}{\partial \delta_i^2} \Delta\delta_i^2 + O(\delta_i^3) \right]_{\delta_{si}} = \boldsymbol{0} \tag{13}$$

When $\boldsymbol{u}$ is the singular vector $\boldsymbol{u}_s$, the inner product of $\boldsymbol{u}_s$ and the first term of the right-hand side in Eq. (13) becomes zero. In addition, by recalling that

$$\frac{\partial^2 \boldsymbol{H}_i}{\partial \delta_i^2} = -\boldsymbol{H}_i \tag{14}$$

and ignoring the terms higher than the second order, the inner product of $\boldsymbol{u}_s$ and Eq. (13) becomes

$$\boldsymbol{u}_s^T \delta \boldsymbol{h} = \boldsymbol{u}_s^T \sum_{i=1}^{4} \left[-\frac{1}{2} \boldsymbol{H}_i \Delta\delta_i^2 \right]_{\delta_{si}} = 0 \tag{15}$$

This constraint equation can be rewritten as

$$\Delta\boldsymbol{\delta}^T \boldsymbol{E} \Delta\boldsymbol{\delta} = 0 \tag{16}$$

where

$$\boldsymbol{E} = \mathrm{diag}(e_1, e_2, e_3, e_4) \tag{17}$$

When the gimbal angles are in the singular configuration, the dimension of the null space is two. Therefore, the null motion of the gimbal angles can be expressed in terms of the null space basis vectors of the Jacobian matrix, $\boldsymbol{n}_i$, as follows:

$$\Delta\delta = \sum_{i=1}^{2} \lambda_i \boldsymbol{n}_i = \boldsymbol{N}\boldsymbol{\lambda} \tag{18}$$

where λ_i is the i^{th} weighting coefficient, and $\boldsymbol{\lambda} = (\lambda_1, \lambda_2)$. Substituting Eq. (18) into Eq. (16) yields

$$\boldsymbol{\lambda}^T \boldsymbol{M} \boldsymbol{\lambda} = 0 \tag{19}$$

where $\boldsymbol{M} = \boldsymbol{N}^T \boldsymbol{E} \boldsymbol{N}$.

If $\boldsymbol{M}$ is sign-definite, then there is no solution to Eq. (19) other than $\boldsymbol{\lambda} = \boldsymbol{0}$. In this case, null motion is impossible at the corresponding singularity. This type of singularity is referred to as an elliptic singularity. On the other hand, if $\boldsymbol{M}$ is indefinite or semidefinite, then there is a solution to Eq. (19) that satisfies $\boldsymbol{\lambda} \neq \boldsymbol{0}$ (i.e., null motion is possible at the singularity). This type of singularity is referred to as a hyperbolic singularity. Note that there are degenerate hyperbolic singularities that cannot be avoided by null motion.

To obtain precise and smooth singular surfaces, the singular vector $\boldsymbol{u}_s$ is chosen radially around the gimbal axis direction. Figures 4 and 5 show the passable and impassable singular surfaces, respectively, corresponding to each skew angle. The singular surfaces are symmetric with respect to the $x = 0$, $y = 0$, and $z = 0$ planes. In addition, the internal singular surfaces have a trumpetlike shape along the gimbal axis directions. These trumpetlike shapes are related to the angle $\epsilon_i \tan^{-1}(\cos\beta)$, in which ϵ_i changes its sign. By comparing the impassable singular surfaces with each other, it is easily seen that the impassable singular surface area becomes wide or narrow depending on the skew angle. If the existence domain of the impassable singular surfaces is small, such a situation with its skew-angle dependence is desired for singularity avoidance.

Wie presented a technique to calculate and visualize singular gimbal angles and singular surfaces[32]. However, he did not illustrate the map of the singular gimbal angles corresponding to the impassable singularities. Figure 6 shows the mapping of the impassable and passable gimbal angle regions, where the red and blue regions correspond to the impassable and passable singular gimbal angles, respectively. By referring to the method in [32], the singular gimbal angles (θ_2, θ_4) are determined from the pair of gimbal angles (θ_1, θ_3), then the passability for the singular gimbal angles is determined, recorded, and illustrated as the passability region map. As shown in Fig. 6, the regions of impassable singular gimbals radiate towards four directions from some sets of gimbal angles, i.e., $(\delta_1, \delta_3) = (\pi/2, \pi/2)$, $(\delta_1, \delta_3) = (3\pi/2, 3\pi/2)$, $(\delta_1, \delta_3) = (\pi/2, 3\pi/2)$, and $(\delta_1, \delta_3) = (3\pi/2, \pi/2)$. The singular surfaces corresponding to these singular gimbals are located around the z or x axis. In addition, the regions of impassable singular gimbals radiate from a gimbal angle of $\tan^{-1}(\cos\beta)$, which correspond to the center of the trumpetlike-shaped parts. If the regions corresponding to the impassable singularities are calculated and recorded in advance, mapping

of these regions can be used to predict how much perturbation of the gimbal angles is required in order to avoid impassable singularities. In other words, the region map can be used for real-time gimbal path planning to avoid impassable singularities. Such a gimbal path planning is beyond the objective of this study.

The surface area of each singularity was calculated by making triangle meshes on the singular surfaces, and integrating the areas of those triangle meshes. Figure 7 shows the relationship between the surface area of each singular surface and each skew angle. To validate this numerical result, the 4H singular surface area was calculated in another way for a few cases of skew angle. By taking into consideration that the 4H singular surface for 2-SPEED CMG ($\beta = \pi/2$) is expressed by $\boldsymbol{h} = (2\cos p, 2\cos q, \pm 2(\sin p + \sin q))^T,\ p, q \in [0, \pi]$, the 4H singular surface area for $\beta = \pi/2$ can be calculated as

$$S_{4H,\beta=\frac{\pi}{2}} = 2\int_0^\pi \int_0^\pi \left| \frac{\partial \boldsymbol{h}}{\partial p} \times \frac{\partial \boldsymbol{h}}{\partial q} \right| dpdq = 8\int_0^\pi \int_0^\pi \sqrt{\sin^2 p + \cos^2 p \sin^2 q} dpdq \simeq 66.48.$$

When the skew angle is infinitesimally near $\pi/2$, the 4H singular surface approximately contains the 4H singular surface of the 2-SPEED CMG and four flat circular plates with radius of 2, each of which has two circular windows with radius of 1. Thus, the 4H singular surface area for $\beta \approx \pi/2$ is given by

$$S_{4H,\beta\approx\frac{\pi}{2}} \simeq S_{4H,\beta=\frac{\pi}{2}} + 4 \times \pi 2^2 - 8 \times \pi 1^2 = 66.48 + 8\pi = 91.58.$$

On the other hand, when β approaches 0, the 4H singular surface becomes a thin pancake-like shape, the top and bottom surfaces of which have four circular windows with radius of 1. Thus, the 4H singular surface area approaches

$$S_{4H,\beta\approx 0} = 2 \times \pi 4^2 - 8 \times \pi 1^2 = 24\pi = 75.36.$$

These values agree with the results indicated in Fig. 7 with respect to the 4H singular surface area.

When the skew angle β is the traditional skew angle (54.73 deg), the impassable singular surface area is minimum, and the 4H singular surface area is maximum. The result of this numerical calculation agrees with the apparatus of the impassable singular surfaces shown in Fig. 5.

From this viewpoint, a pyramid-type CMG with the traditional skew angle might be the best configuration for avoiding encountering the impassable singularities as much as possible. Despite this fact, we intentionally propose the adaptive-skew CMG to obtain a larger torque by treating the skew angle as one of the variable parameters.

It is shown in Fig. 6(c) that when the skew angle is $\beta = 80$ deg, the impassable region in the gimbal coordinate is small, compared to that of $\beta = 10$ deg and $\beta = 54.73$ deg. This result seems to contradict the result presented in Fig. 5(c). Note that although there are 16 sets of the singular gimbal angles, Fig. 6(c) shows a part of the region map for the singular gimbals.

Next, singularities of the ASCMGs will be analyzed from the viewpoint of the freedom of the skew angle to change.

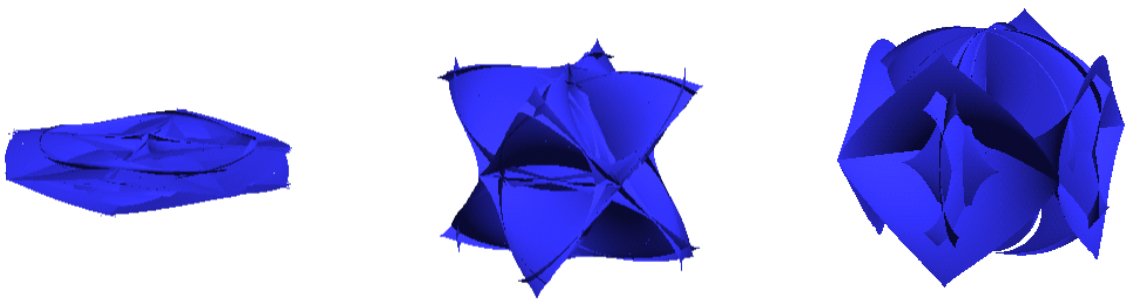

(a) (b) (c)

Figure 4: Passable singular surfaces for (a) $\beta = 10$ deg, (b) $\beta = 54.73$ deg, and (c) $\beta = 80$ deg.

3.2. Analysis of ASCMG Singularities

Although there is a degree of freedom associated with the skew angle, singularities still exist for the ASCMGs. This is because, in contrast to the DGCMGs, the skew angles among the four CMGs are not independently changeable, but are strictly controlled to maintain a consistent angle among the four CMG units of the ASCMG system. The singularities for the traditional fixed-skew CMGs are not always identical to the singularities of the ASCMGs, due to the degree of freedom for the skew angle. In this subsection, singularities of the ASCMGs are analyzed by taking this degree of freedom into consideration.

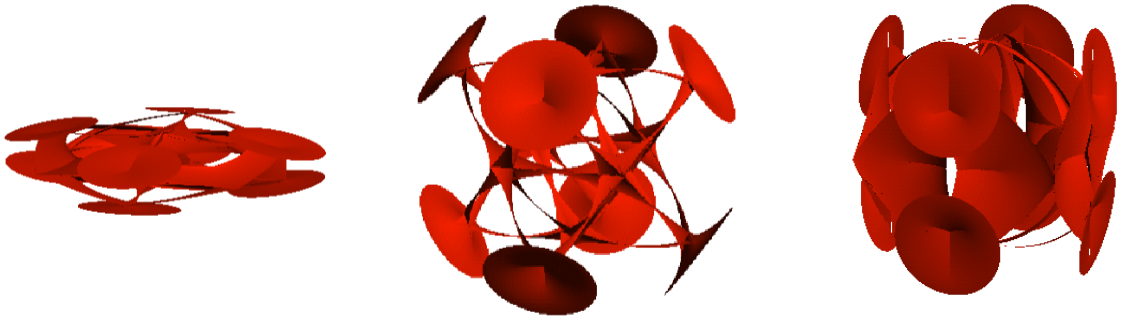

(a) (b) (c)

Figure 5: Impassable singular surfaces for (a) $\beta = 10$ deg, (b) $\beta = 54.73$ deg, and (c) $\beta = 80$ deg.

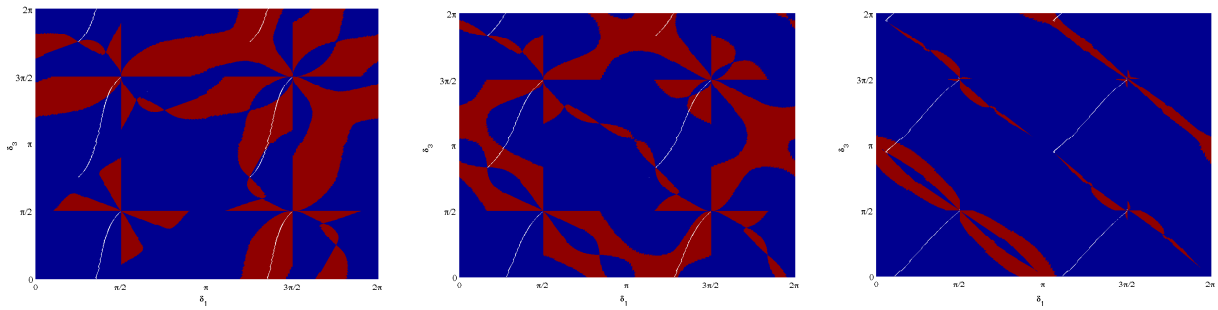

(a) (b) (c)

Figure 6: Mapping of impassable (red) and passable (blue) regions of the singular gimbal angles for (a) $\beta = 10$ deg, (b) $\beta = 54.73$ deg, and (c) $\beta = 80$ deg.

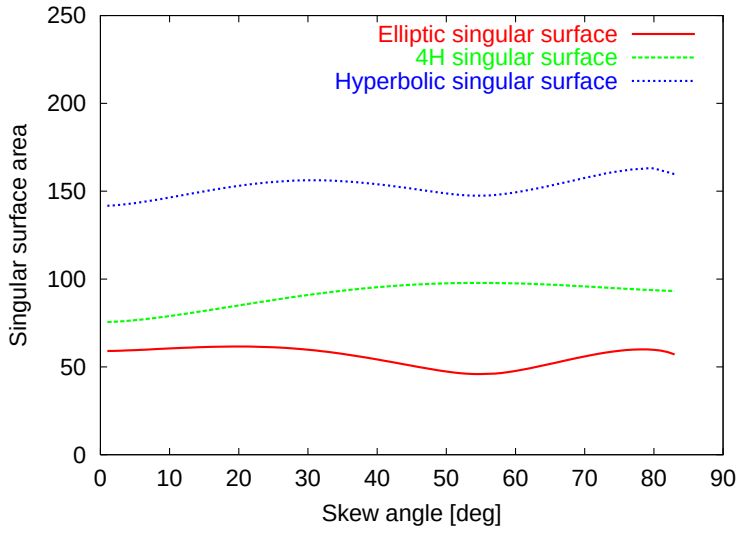

Figure 7: Surface area of each singularity vs. skew angle.

Similar to the definition of singularities for the fixed-skew CMGs, a singularity of the ASCMGs is defined as a situation in which the CMG system cannot produce any momentum vector change along the specified direction of $\boldsymbol{u}_s$, which is referred to as the singular vector.

By taking into consideration that both the gimbal angles and skew angle are control variables in the ASCMGs, the time derivative of the angular momentum vector of the ASCMGs (Eq.(2)) is expressed by

$$\dot{\boldsymbol{h}} = \sum_{i=1}^{4} \frac{\partial \boldsymbol{H}_i}{\partial \delta_i} \dot{\delta}_i + \sum_{i=1}^{4} \frac{\partial \boldsymbol{H}_i}{\partial \beta} \dot{\beta} = \begin{bmatrix} \boldsymbol{C} & \boldsymbol{D} \end{bmatrix} \begin{bmatrix} \dot{\boldsymbol{\delta}} \\ \dot{\beta} \end{bmatrix} = \boldsymbol{Q} \begin{bmatrix} \dot{\boldsymbol{\delta}} \\ \dot{\beta} \end{bmatrix} \tag{20}$$

where $\boldsymbol{D}$ is

$$\boldsymbol{D} = \begin{bmatrix} (\sin\delta_1 - \sin\delta_3)\, s\beta \\ (\sin\delta_2 - \sin\delta_4)\, s\beta \\ (\sin\delta_1 + \sin\delta_2 + \sin\delta_3 + \sin\delta_4)\, c\beta \end{bmatrix} \tag{21}$$

Similarly, by differentiating the momentum vector of the ASCMGs (Eqs.(6), (7) and (8)) with respect to

the skew angle, we have

$$
\begin{aligned}
H_{x\beta} &= \frac{-s\beta(-s\beta u_z + c\beta u_x) + c\beta(-c\beta u_z - s\beta u_x)}{e_1} - \frac{c\beta(-s\beta u_z + c\beta u_x)e_{1\beta}}{e_1^2} - \frac{u_x e_{2\beta}}{e_2^2} \\
&\quad + \frac{-s\beta(s\beta u_z + c\beta u_x) + c\beta(c\beta u_z - s\beta u_x)}{e_3} - \frac{c\beta(s\beta u_z + c\beta u_x)e_{3\beta}}{e_3^2} - \frac{u_x e_{4\beta}}{e_4^2} \qquad (22) \\
H_{y\beta} &= -\frac{u_y e_{1\beta}}{e_1^2} - \frac{s\beta(-s\beta u_z + c\beta u_y) + c\beta(c\beta u_z + s\beta u_y)}{e_2} \\
&\quad - \frac{c\beta(-s\beta u_z + c\beta u_y)e_{2\beta}}{e_2^2} - \frac{u_y e_{3\beta}}{e_3^2} + \frac{-s\beta(s\beta u_z + c\beta u_y) + c\beta(c\beta u_z - s\beta u_y)}{e_4} \\
&\quad - \frac{c\beta(s\beta u_z + c\beta u_y)e_{4\beta}}{e_4^2} \qquad (23) \\
H_{z\beta} &= \frac{c\beta(-c\beta u_x + s\beta u_z) + s\beta(s\beta u_x + c\beta u_z)}{e_1} - \frac{s\beta(-c\beta u_x + s\beta u_z)e_{1\beta}}{e_1^2} \\
&\quad + \frac{c\beta(s\beta u_z - c\beta u_y) + s\beta(c\beta u_z + s\beta u_y)}{e_2} - \frac{s\beta(s\beta u_z - c\beta u_y)e_{2\beta}}{e_2^2} \\
&\quad + \frac{c\beta(s\beta u_z + c\beta u_x) + s\beta(c\beta u_z - s\beta u_x)}{e_3} - \frac{s\beta(s\beta u_z + c\beta u_x)e_{3\beta}}{e_3^2} \\
&\quad + \frac{c\beta(s\beta u_z + c\beta u_y) + s\beta(c\beta u_z - s\beta u_y)}{e_4} - \frac{s\beta(s\beta u_z + c\beta u_y)e_{4\beta}}{e_4^2} \qquad (24)
\end{aligned}
$$

where

$$
\begin{aligned}
e_{1\beta} &= \pm\frac{(s\beta u_x + c\beta u_z)(-c\beta u_x + s\beta u_z)}{\sqrt{1 - (s\beta u_x + c\beta u_z)^2}} \qquad (25) \\
e_{2\beta} &= \pm\frac{(s\beta u_y + c\beta u_z)(-c\beta u_y + s\beta u_z)}{\sqrt{1 - (s\beta u_y + c\beta u_z)^2}} \qquad (26) \\
e_{3\beta} &= \pm\frac{(-s\beta u_x + c\beta u_z)(c\beta u_x + s\beta u_z)}{\sqrt{1 - (-s\beta u_x + c\beta u_z)^2}} \qquad (27) \\
e_{4\beta} &= \pm\frac{(-s\beta u_y + c\beta u_z)(c\beta u_y + s\beta u_z)}{\sqrt{1 - (-s\beta u_y + c\beta u_z)^2}} \qquad (28)
\end{aligned}
$$

There are two methods for obtaining a set of singular gimbal angles and skew angle. One is based on the method in [32], and the other is a method using Eqs. (22), (23), and (24).

In the former method, based on the method in [32], singular gimbal angles of the CMGs are determined for the given skew angle, and then taking into consideration the singular condition associated with the skew angle, i.e., $\det(\boldsymbol{Q}\boldsymbol{Q}^{\mathrm{T}}) = 0$, or alternative simple condition $\boldsymbol{u}_s^T \boldsymbol{D} = 0$, the singular skew angle can be obtained by numerical techniques such as the Newton-Rapson or bi-section method.

In the latter method, for the given singular vector $\boldsymbol{u}_s$, the condition for the singularities of the ASCMGs is given by

$$u_x H_{x\beta} + u_y H_{y\beta} + u_z H_{z\beta} = 0 \tag{29}$$

By solving this equation with respect to the skew angle numerically, the singular skew angle corresponding to the singular vector $\boldsymbol{u}_s$ can be obtained. Although there is no fundamental difference between the above two methods, the latter method is employed in this study because of its ease of implementation.

Figure 8(a) shows the singular skew angles for the 4H singularities ($\varepsilon_i = (+,+,+,+)$), corresponding to the singular vector expressed in the form of the spherical polar coordinate angles (θ_1, θ_2). Note that the illustrated region is clipped to within $\theta_1 \in [0, \pi/2]$ and $\theta_2 \in [0, \pi/4]$ because the pyramid-type CMG is symmetric with respect to the $x = y$ and $x = -y$ planes. It should be noted that more than one singular skew angle exist for the singular vector. One of them is constant in $\pi/2$, indicated in green in the figure, for which the ASCMG system becomes identical to the 2-SPEED CMG. The other singular skew angle varies in accordance with the singular vector. Singular skew angles other than $\pi/2$ for the 4H singularities do not exist for singular vectors in some domains of (θ_1, θ_2). Contrary to the fixed-skew CMGs in which there exists only one 4H singular momentum corresponding to the specified singular vector, there are two singular skew angles other than $\pi/2$ for the 4H singularities corresponding to the singular vector in some domains for the ASCMGs. This implies that two 4H singular momenta exist for one singular vector in such a domain for the ASCMGs. This fact will be explained geometrically in the next subsection. The number of singular gimbal angles for the fixed-skew pyramid-array CMGs is given by $2^n (= 2^4 = 16)$, whereas the number of singular gimbals for the ASCMGs can be neither given by $2^5 (= 32)$ nor $2^4 (= 16)$, because the skew angle is related to all the gimbal vectors and cannot be simply treated as one of the independent gimbals. In other words, in the fixed-skew CMGs, the gimbal angles opposite to the singular gimbal angles are also always singular gimbal angles. However, this does not always apply to the ASCMGs due to the freedom of the skew angle. Figure 8(b) shows the singular skew angles for the 2H internal singularities ($\varepsilon_i = (+,-,+,+)$). Comparing Fig. 8(a) with Fig. 8(b), it is found that the singular skew angles for the 4H singularities are not always the same as that for the internal singularities.

Figure 9(a) and (b) shows the internal singularities projected onto the x–z and x–y planes, respectively.

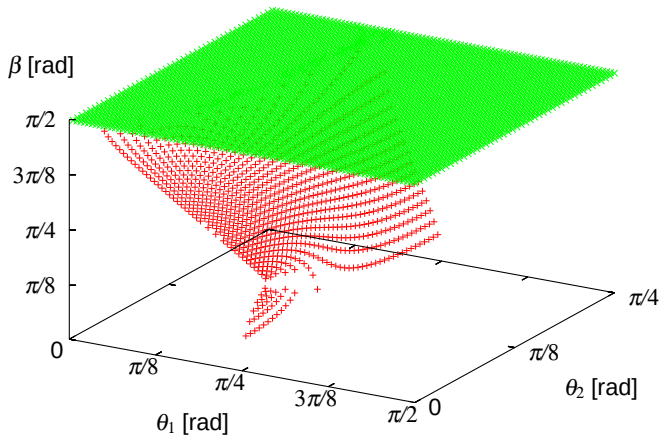

(a) for 4H singularities ($\varepsilon_i = (+,+,+,+)$)

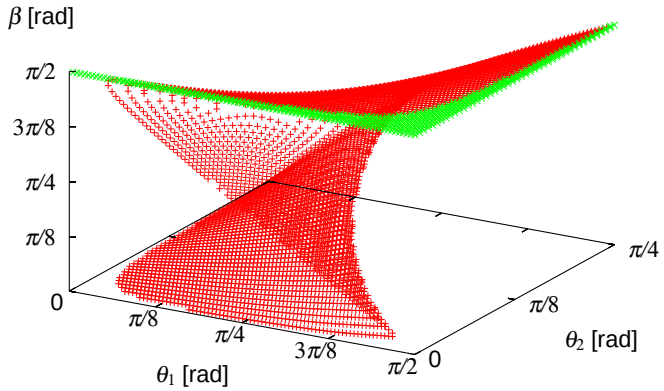

(b) for 2H internal singularities ($\varepsilon_i = (+,-,+,+)$)

Figure 8: Singular skew angle.

Although there are four flat circular windows for the 2-SPEED CMG representing the 2H singular surfaces, those windows are not included as singular surfaces for the ASCMGs because of the degree of freedom associated with the skew angle. It is shown in Fig. 9(a) that the singularities observed from the side view contain half-circular curves, which correspond to the 0H singular surfaces of the 2-SPEED CMG. This implies that the 0H singular surfaces of the 2-SPEED CMG are also singular surfaces of the ASCMGs. This is because the Jacobian $\boldsymbol{D}$ related to the skew angle is a zero vector when the skew angle is $\pi/2$, and the gimbal angles correspond to the 0H singular surfaces of the 2-SPEED CMG. It can also be seen in Fig. 9(a) that the singularities observed from the side view contain asteroid curves. The reason why asteroid curves (surfaces) are included in the side view can be explained as follows. When the 0H singularities of the CMG with a skew angle β are viewed from the side, those singularities contain lines connecting two points: $(\pm 2\cos\beta, 0)$ and $(0, \pm 2\sin\beta)$. For the case in which the skew angle β varies as $0 < \beta \leq \pi/2$, the envelope curves for the above lines result in asteroid curves. The envelope curves are singularities for the ASCMGs because the singular characteristics and the rank of the Jacobian do not change at any point on the envelope curves when subjected to an infinitesimal change in the skew angle.

3.3. Projection of the Momentum Envelope of the ASCMGs on the x–z plane

The momentum envelope of the ASCMGs can be defined as the envelope that covers the momentum of a pyramid-type CMG whose skew angle varies from 0 to $\pi/2$ rad. For the fixed-skew CMG, the singular momentum projection on the x-z plane is expressed as[32]

$$\frac{H_x^2}{4} + \frac{(H_z \pm 2\sin\beta)^2}{(2\sin\beta)^2} = 1, (0 < \beta \leq \pi/2 \text{ rad}) \tag{30}$$

$$\frac{(H_x \pm 2\cos\beta)^2}{4} + \frac{H_z^2}{(2\sin\beta)^2} = 1, (0 < \beta \leq \pi/2 \text{ rad}) \tag{31}$$

When $\beta = \pi/2$, $\delta_1 = \delta_3 = \pm\pi/2$, and $\delta_2 = \pi - \delta_4$; or when $\beta \neq \pi/2$, $\delta_1 = \delta_3 = \pm\pi/2$, and $\sin\delta_2 = \sin\delta_4 = 0$; it can be easily found that the rank of the Jacobian $\boldsymbol{Q}$ is two. From this point of view, the envelope curves of Eq. (30) form a part of the ASCMGs' momentum envelope that results from cutting the momentum envelope in the x–y plane and projecting it onto the x–y plane. In order to obtain analytical expressions of these curves, we calculate the envelope curves of Eqs. (30) and (31) as follows.

First, let us consider the envelope curves of Eq. (30). By partially differentiating Eq. (30) with

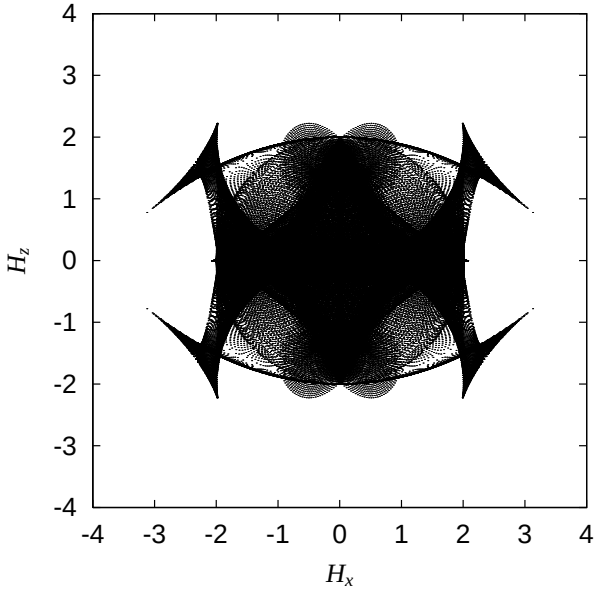

(a) side view

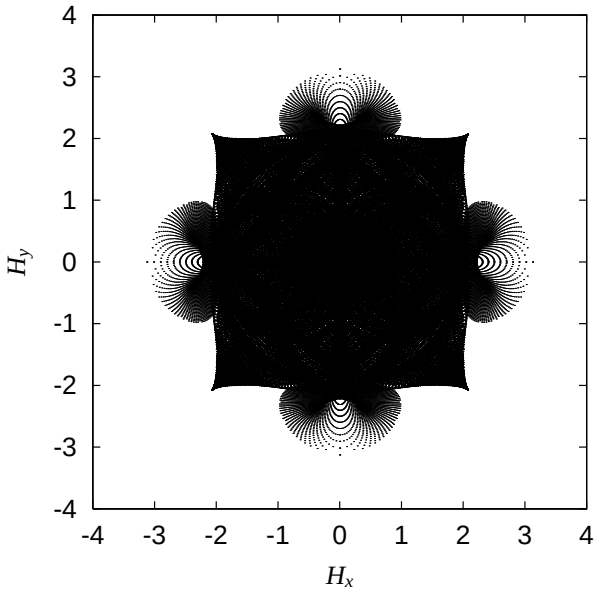

(b) top view

Figure 9: Internal singularities of ASCMGs.

respect to β and solving for β, we obtain $\beta = \pi/2$ or $\beta = \csc^{-1}(2/H_z)$, and H_z must be less than or equal to 2 so that a real value of β can exist. As mentioned above, when $\beta = \pi/2$, $\delta_1 = \delta_3 = \pm\pi/2$, and $\delta_2 = \pi - \delta_4$, these angles are included in the singularities of the ASCMGs, and the corresponding singularities are the 4H singularities of the 2-SPEED CMG. Substituting the resulting β into Eq. (30), we can obtain the envelope curves expressed by

$$H_x = \pm 2, |H_z| \leq 2 \tag{32}$$

$$H_x^2 + (H_z \pm 2)^2 = 4 \tag{33}$$

This implies that the 4H singular momentum of the 2-SPEED CMG projected onto the x–z plane is a part of the momentum envelope of the ASCMGs. This fact can be confirmed in that the momentum envelope of the ASCMGs above the $z = 2$ plane and below the $z = -2$ plane has the same shape as that of the 2-SPEED CMG.

Next, the envelope curves of Eq. (31) are considered. Similar to the above case, by partially differentiating Eq. (31) with respect to β and solving for $\cos\beta$, we obtain $\cos\beta = H_x/4$ and $\cos\beta = \left(H_x \pm \sqrt{H_x^2 + 16}\right)/4$. The second solution, however, has no meaning because we assume that $0 < \beta \leq \pi/2$, and thus, $0 \leq \cos\beta < 1$ under this assumption. Therefore, substituting the first solution into Eq. (31) and simplifying the equation, we can obtain the envelope curves as follows:

$$H_z = \pm\left(2 - \frac{H_x^2}{8}\right), |H_x| \geq 2 \tag{34}$$

Summarizing Eqs. (32), (33), and (34), the x–z plane section of the momentum envelope of the ASCMGs is as shown in Fig. 10(a).

Figure 10(b) shows the momentum envelope of the ASCMGs in the form of a three-dimensional shaded surface. The momentum envelope shape of the ASCMGs in the z direction is hemispherical, whereas the shape in the x (and y) direction is an obtuse angle. Four dimples are observed, and they are similar to those of the momentum envelope of the traditional fixed-skew pyramid CMG. However, the normal direction of the momentum envelope around the dimples for the ASCMGs is different from that of the fixed-skew CMG.

To explain that there exist more than one 4H singularity corresponding to a singular vector, three arrows corresponding to the singular vector are shown in Fig. 10(b), where the root of the arrow is located on the corresponding 4H singular momentum. One of the arrows corresponds to singular skew angle $\beta = \pi/2$ rad, and the other two arrows correspond to singular skew angles other than $\beta = \pi/2$ rad.

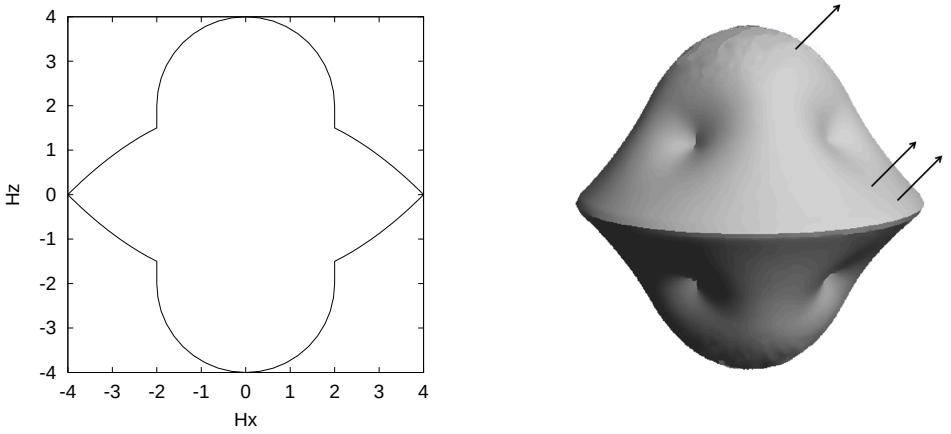

(a) x-z plane section (b) three-dimensional shaded surface

Figure 10: Momentum envelope of ASCMGs.

3.4. Passability of ASCMGs Singularities by Null Motion

Similar to the fixed-skew CMGs, the internal singularities of the ASCMGs consist of hyperbolic and elliptic singularities. In this subsection, we will analyze whether the internal singularities are hyperbolic or elliptic, that is, whether null motion is possible or impossible. The analytical method for determining the ASCMGs' type of singularity is basically the same as that of the fixed-skew pyramid CMG, but we need to consider that there are not four but five degrees of freedom in the ASCMGs because of the adaptive skew angle.

The condition for null motion of the ASCMGs can be expressed using a Taylor series as follows:

$$\begin{aligned} \delta \boldsymbol{h} \;=\; & \sum_{i=1}^{4} \left[\frac{\partial \boldsymbol{H}_i}{\partial \delta_i} \Delta\delta_i + \frac{\partial \boldsymbol{H}_i}{\partial \beta} \Delta\beta + \frac{1}{2} \left\{ \frac{\partial^2 \boldsymbol{H}_i}{\partial \delta_i^2} \Delta\delta_i^2 + \frac{\partial^2 \boldsymbol{H}_i}{\partial \beta^2} \Delta\beta^2 + 2 \frac{\partial^2 \boldsymbol{H}_i}{\partial \beta \partial \delta_i} \Delta\beta\Delta\delta_i \right\} \right. \\ & \left. + O^3(\delta_i, \beta) \right]_{\delta_{si}, \beta_s} = \boldsymbol{0} \end{aligned} \tag{35}$$

Recalling Eq. (20), Eq. (35) can be written as

$$\delta \boldsymbol{h} = \boldsymbol{Q} \begin{bmatrix} \Delta\boldsymbol{\delta} \\ \Delta\beta \end{bmatrix} + \sum_{i=1}^{4} \left[\frac{1}{2} \left\{ \frac{\partial^2 \boldsymbol{H}_i}{\partial \delta_i^2} \Delta\delta_i^2 + \frac{\partial^2 \boldsymbol{H}_i}{\partial \beta^2} \Delta\beta^2 + 2 \frac{\partial^2 \boldsymbol{H}_i}{\partial \beta \partial \delta_i} \Delta\beta \Delta\delta_i \right\} + O^3(\delta_i, \beta) \right]_{\delta_{si}, \beta_s} = \boldsymbol{0} \tag{36}$$

When $\boldsymbol{u}$ is the singular vector $\boldsymbol{u}_s$, the inner product of $\boldsymbol{u}_s$ and the first term on the right-hand side of Eq. (36) becomes zero. Recalling Eq. (14) and ignoring terms higher than the second order, the inner product of $\boldsymbol{u}_s$ and Eq. (36) becomes

$$\boldsymbol{u}_s^T \delta \boldsymbol{h} = \boldsymbol{u}_s^T \sum_{i=1}^{4} \left[\frac{1}{2} \left\{ -\boldsymbol{H}_i \Delta\delta_i^2 + \frac{\partial^2 \boldsymbol{H}_i}{\partial \beta^2} \Delta\beta^2 + 2 \frac{\partial^2 \boldsymbol{H}_i}{\partial \beta \partial \delta_i} \Delta\beta \Delta\delta_i \right\} \right]_{\delta_{si}, \beta_s} = 0 \tag{37}$$

This constraint equation can be rewritten as

$$\left[\Delta\boldsymbol{\delta}^T, \Delta\beta \right] \begin{bmatrix} \boldsymbol{E} & -\boldsymbol{F}^T \\ -\boldsymbol{F} & -b \end{bmatrix} \begin{bmatrix} \Delta\boldsymbol{\delta} \\ \Delta\beta \end{bmatrix} = \left[\Delta\boldsymbol{\delta}^T, \Delta\beta \right] \boldsymbol{E}' \begin{bmatrix} \Delta\boldsymbol{\delta} \\ \Delta\beta \end{bmatrix} = 0 \tag{38}$$

where

$$\boldsymbol{F} = \boldsymbol{u}_s^T \left[\frac{\partial^2 \boldsymbol{H}_1}{\partial \delta_1 \partial \beta}, \frac{\partial^2 \boldsymbol{H}_2}{\partial \delta_2 \partial \beta}, \frac{\partial^2 \boldsymbol{H}_3}{\partial \delta_3 \partial \beta}, \frac{\partial^2 \boldsymbol{H}_4}{\partial \delta_4 \partial \beta} \right] \tag{39}$$

$$b = \boldsymbol{u}_s^T \sum_{i=1}^{4} \frac{\partial^2 \boldsymbol{H}_i}{\partial \beta^2} \tag{40}$$

When a set of gimbal and skew angles is in the singular state, the rank of the Jacobian $\boldsymbol{Q}$ is two, and the dimension of the null space is $n - \mathrm{rank}(\boldsymbol{Q}) = 5 - 2 = 3$. Therefore, the null motion of the set of gimbal and skew angles can be expressed in terms of the null space basis vectors of the Jacobian matrix $\boldsymbol{n}_i'$ as follows:

$$\begin{bmatrix} \Delta\boldsymbol{\delta} \\ \Delta\beta \end{bmatrix} = \sum_{i=1}^{3} \lambda_i' \boldsymbol{n}_i' = \boldsymbol{N}' \boldsymbol{\lambda}' \tag{41}$$

where λ_i' is the i^{th} weighting coefficient, and $\boldsymbol{\lambda}' = (\lambda_1', \lambda_2', \lambda_3')$. Substituting Eq. (41) into Eq. (38) yields

$$\boldsymbol{\lambda}'^T \boldsymbol{M}' \boldsymbol{\lambda}' = 0 \tag{42}$$

where $\boldsymbol{M}' = \boldsymbol{N}'^T \boldsymbol{E}' \boldsymbol{N}' \in \mathcal{R}^{3\times 3}$. If $\boldsymbol{M}'$ is sign-definite, then there is no solution to Eq. (42) other than $\boldsymbol{\lambda}' = \boldsymbol{0}$. In this case, null motion is impossible at the corresponding singularity for the ASCMGs. On the other hand, if $\boldsymbol{M}'$ is indefinite or semidefinite, then there is a solution to Eq. (42) that satisfies $\boldsymbol{\lambda}' \neq \boldsymbol{0}$; that is, null motion is possible at the singularity for the ASCMGs.

Figures 11(a) shows the elliptic singularities of the ASCMGs. The trumpet-like shapes are located around the intersection between the 4H singularities of the 2-SPEED CMG and the singularities expressed by Eq. (33), and they correspond to the dimples in the momentum envelope of the ASCMGs. The topological structure of the elliptic singularities is the same as that of the fixed-skew CMG. However, the direction of the trumpet-like shape is different from that of the traditional fixed-skew pyramid-array CMGs, and the trumpet-like shapes are not circular, but elliptic for the ASCMGs, whereas they are circular for the fixed-skew CMGs. Figure 11(b) shows the hyperbolic singularities of the ASCMGs. The hyperbolic singularities of the ASCMGs contain the 0H singularities of the 2-SPEED CMG, but some of them are located outside the range of the 0H singularities of the 2-SPEED CMG. These are the main differences of the internal singularities of the ASCMGs from that of the fixed-skew pyramid-array CMGs due to the degree of freedom of the skew angle.

4. Steering Control Laws

4.1. Quaternion Feedback Control Law

By introducing the internal control torque vector generated by the CMGs and denoted by $\boldsymbol{u}_c = (u_1, u_2, u_3)^T$, the equations of motion for the spacecraft and the CMGs are written, respectively, as

$$\boldsymbol{J}\dot{\boldsymbol{\omega}} + \boldsymbol{\omega} \times \boldsymbol{J}\boldsymbol{\omega} = \boldsymbol{u}_c + \boldsymbol{T}_{\text{ext}} \tag{43}$$

$$\dot{\boldsymbol{h}} + \boldsymbol{\omega} \times \boldsymbol{h} = -\boldsymbol{u}_c \tag{44}$$

where $\boldsymbol{T}_{\text{ext}}$ is an external torque affecting the spacecraft. Provided that the spacecraft control torque input $\boldsymbol{u}_c$ is given by some attitude control laws, the desired CMG momentum rate is often selected as

$$\dot{\boldsymbol{h}} = -\boldsymbol{u}_c - \boldsymbol{\omega} \times \boldsymbol{h} \tag{45}$$

Defining a quaternion vector $\boldsymbol{q}(=(q_1, q_2, q_3, q_4)^T = (\hat{\boldsymbol{q}}^T,\ q_4)^T)$ as

$$\boldsymbol{q} = \begin{bmatrix} \hat{\boldsymbol{q}} \\ q_4 \end{bmatrix} = \begin{bmatrix} \hat{\boldsymbol{e}} \sin(\varphi/2) \\ \cos(\varphi/2) \end{bmatrix} \tag{46}$$

where $\hat{\boldsymbol{e}}$ is the eigenaxis unit vector for rotation, and φ is the rotational angle around the eigenaxis vector. The direct cosine matrix from the inertia frame to the spacecraft's body frame $\boldsymbol{R}$ is given by

$$\boldsymbol{R} = \begin{bmatrix} 1-2(q_2^2+q_3^2) & 2(q_1q_2+q_3q_4) & 2(q_1q_3-q_2q_4) \\ 2(q_1q_2-q_3q_4) & 1-2(q_1^2+q_3^2) & 2(q_2q_3+q_1q_4) \\ 2(q_1q_3+q_2q_4) & 2(q_2q_3-q_1q_4) & 1-2(q_1^2+q_2^2) \end{bmatrix} \tag{47}$$

The differential equations describing the quaternion kinematics are given by

$$\dot{\boldsymbol{q}} = \frac{1}{2} \begin{bmatrix} q_4\boldsymbol{\omega} - \boldsymbol{\omega} \times \hat{\boldsymbol{q}} \\ -\boldsymbol{\omega}^T \hat{\boldsymbol{q}} \end{bmatrix} \tag{48}$$

Because a quaternion vector is well suited to on-board real-time computation and has no singular points, the following quaternion-feedback control[2] can be considered for real-time implementation for determining the command control torque and is used in this study:

$$\boldsymbol{u}_c = -\boldsymbol{K}_p \hat{\boldsymbol{q}}_e - \boldsymbol{K}_d \boldsymbol{\omega} \tag{49}$$

where $\boldsymbol{K}_p$ and $\boldsymbol{K}_d$ are the control gain matrices. The attitude error quaternions $(q_{e1}, q_{e2}, q_{e3}, q_{e4})$ are computed using the desired or commanded attitude quaternions $(q_{c1}, q_{c2}, q_{c3}, q_{c4})$ and the current attitude quaternions (q_1, q_2, q_3, q_4) as follows:

$$\begin{bmatrix} q_{e1} \\ q_{e2} \\ q_{e3} \\ q_{e4} \end{bmatrix} = \begin{bmatrix} q_{c4} & q_{c3} & -q_{c2} & -q_{c1} \\ -q_{c3} & q_{c4} & q_{c1} & -q_{c2} \\ q_{c2} & -q_{c1} & q_{c4} & -q_{c3} \\ q_{c1} & q_{c2} & q_{c3} & q_{c4} \end{bmatrix} \begin{bmatrix} q_1 \\ q_2 \\ q_3 \\ q_4 \end{bmatrix} \tag{50}$$

4.2. Steering Control Laws

In this section, three steering control laws are described: the generalized singularity robust (GSR) inverse for the fixed-skew CMGs, the GSR for the ASCMGs, and the GSR plus null motion for the ASCMGs.

4.2.1. GSR Inverse for Fixed-skew CMGs

The GSR inverse is expressed as[10, 11]

$$\dot{\boldsymbol{\delta}} = \boldsymbol{C}^T(\boldsymbol{C}\boldsymbol{C}^T + \lambda\boldsymbol{E})^{-1}(\dot{\boldsymbol{h}}/H) \tag{51}$$

where

$$\boldsymbol{E} = \begin{bmatrix} 1 & \epsilon_3 & \epsilon_2 \\ \epsilon_3 & 1 & \epsilon_1 \\ \epsilon_2 & \epsilon_1 & 1 \end{bmatrix} \tag{52}$$

The scalar parameters λ and ϵ_i are set to small values, not to generate a very large torque error, but to avoid singularities. In [10, 11], λ and ϵ_i are given by

$$\lambda = \lambda_0 \exp(-\mu \det(\boldsymbol{C}\boldsymbol{C}^T)), \;\; \lambda_0 > 0, \; \mu > 0 \tag{53}$$

$$\epsilon_i = \epsilon_0 \sin(\omega t + \phi_i) \tag{54}$$

where λ_0 is set to a small value, and ϵ_0, ω, and ϕ are the amplitude, modulation frequency, and phase, respectively, to be appropriately chosen for perturbation.

4.2.2. GSR Inverse for the ASCMGs (AS-GSR)

Referring to the GSR for the fixed-skew CMGs, the GSR inverse logic for the ASCMGs can be implemented as

$$\begin{bmatrix} \dot{\boldsymbol{\delta}} \\ \dot{\beta} \end{bmatrix} = \boldsymbol{W}\boldsymbol{Q}^T \left(\boldsymbol{Q}\boldsymbol{W}\boldsymbol{Q}^T + \lambda\boldsymbol{E}\right)^{-1} (\dot{\boldsymbol{h}}/H) \tag{55}$$

where $\lambda = \lambda_0 \exp(-\mu \det(\boldsymbol{Q}\boldsymbol{Q}^T))$, and $\boldsymbol{W}$ is a weighting matrix that can be used to distribute the command torque between the gimbal rate and skew-angle rate. Hereinafter, this steering law is referred

to as the AS-GSR.

4.2.3. GSR with Null Motion for the ASCMGs (AS-GSR+LG)

Let $\kappa(\boldsymbol{\delta}, \beta)$ denote a condition number of the matrix $\boldsymbol{Q}$ that is a function of the gimbal angles and the skew angle. Referring to the gradient control law for the VSGCMGs[22], a steering control law using null motion for the ASCMGs can be written as

$$\begin{bmatrix} \dot{\boldsymbol{\delta}} \\ \dot{\beta} \end{bmatrix} = \boldsymbol{W}\boldsymbol{Q}^T \left(\boldsymbol{Q}\boldsymbol{W}\boldsymbol{Q}^T + \lambda \boldsymbol{E}\right)^{-1} (\dot{\boldsymbol{h}}/H) + \boldsymbol{\mathcal{N}}\boldsymbol{d}, \quad \boldsymbol{d} \in \mathcal{R}^{5\times 1} \tag{56}$$

$$\boldsymbol{\mathcal{N}} = \left[\boldsymbol{I}_5 - \tilde{\boldsymbol{W}}\boldsymbol{Q}^T \left(\boldsymbol{Q}\tilde{\boldsymbol{W}}\boldsymbol{Q}^T\right)^{-1} \boldsymbol{Q}\right] \tilde{\boldsymbol{W}} \tag{57}$$

where $\tilde{\boldsymbol{W}}$ is a weighting matrix that can be used to distribute the null motion between the gimbal rate and the skew angle rate. It can be easily shown that

$$\boldsymbol{Q}\boldsymbol{\mathcal{N}}\boldsymbol{d} = \boldsymbol{0} \tag{58}$$

that is, $\boldsymbol{\mathcal{N}}\boldsymbol{d}$ is a null motion, and the matrix $\boldsymbol{\mathcal{N}}$ is positive semidefinite if the vector $\boldsymbol{d}$ is selected as

$$\boldsymbol{d} = -k \begin{bmatrix} \left(\dfrac{\partial \kappa}{\partial \boldsymbol{\delta}}\right)^T \\ \left(\dfrac{\partial \kappa}{\partial \beta}\right) \end{bmatrix}, \quad k > 0 \tag{59}$$

As mentioned above, an algorithm to quickly compute $(\partial\kappa/\partial\boldsymbol{\delta})$ is provided in [22]. The other sensitivity $(\partial\kappa/\partial\beta)$ can also be computed in a similar fashion; see also [22]. Hereinafter, the steering control law Eq. (56) is referred to as the AS-GSR+LG.

5. Numerical Simulations

To validate the effectiveness of the ASCMGs, numerical simulations were carried out for both of the ASCMGs and the traditional fixed-skew SGCMGs. The parameters used for the simulations are listed in Table 2. For all simulations, the initial satellite's angular velocities are set to zero, and the goal

attitude is set to the inertial frame, that is, the goal quaternion is given by $\boldsymbol{q} = (0, 0, 0, 1)$. In this paper, two case studies of attitude maneuvers are considered. The initial attitude is given by a quaternion $\boldsymbol{q}(0) = (-1.0, 0, 0, 0)$ for case 1 and $\boldsymbol{q}(0) = (0, 0, -1, 0)$ for case 2. That is, the numerical simulations considered herein are a maneuver of π rad around the x-axis for case 1 and a maneuver of π rad around the z-axis for case 2.

Because the range of the skew angle β is assumed to be $\beta_{\min} \leq \beta \leq \beta_{\max}$, due to the mechanical limitation for the skew angle in the experimental setup, the skewing rate is modified to prevent the skew angle from exceeding the restricted range as follows:

$$\dot{\beta} = \begin{cases} \dot{\beta} & \\ 0 & \text{if } (\beta \geq \beta_{\max} \text{ and } \dot{\beta} > 0) \text{ or } (\beta \leq \beta_{\min} \text{ and } \dot{\beta} < 0) \end{cases} \tag{60}$$

Moreover, taking into consideration the mechanical limitation in the stepper motors used for controlling the gimbal angle and the skew angle, the gimbal rate command and the skew angle rate command are modified as

$$\dot{\delta}_i = \begin{cases} \dot{\delta}_i & \text{if } |\dot{\delta}_i| < \dot{\delta}_{\max} \\ \text{sign}(\dot{\delta})\dot{\delta}_{\max} & \text{otherwise} \end{cases} \tag{61}$$

$$\dot{\beta} = \begin{cases} \dot{\beta} & \text{if } |\dot{\beta}| < \dot{\beta}_{\max} \\ \text{sign}(\dot{\beta})\dot{\beta}_{\max} & \text{otherwise} \end{cases} \tag{62}$$

The skew angle is used not only for generating torque, but also for avoiding or escaping from the singularities. By taking this into consideration, the values of the weighting matrices were chosen so that they did not accelerate the skew angle too much. In this study, a settling condition was defined such that the quaternion error norm was less than 0.001 and the angular velocity was under 0.5 deg/s.

Figures 12, 13, and 14 show the results of the GSR, the AS-GSR, and the AS-GSR+LG for case 1, respectively. The results corresponding to case 2 are shown in Figs. 15 through 17. In each figure, the time responses of the gimbal angles, the attitude in the form of quaternions, the angular velocity of the spacecraft, and the singularity measure are shown. The time responses of the skew angle for the AS-GSR and the AS-GSR+LG are also shown in Figs. 13(e) and 14(e) for case 1 and are shown in Figs. 16(e)

and 17(e) for case 2.

In case 1, the GSR inverse law encountered internal singularities around 5 s, then the angular velocities around y- and z-axes were induced by perturbation torques for singularity avoidance. Similarly, the AS-GSR and the AS-GSR+LG laws encountered internal singularities around 5 s. For the case of the AS-GSR, the skew angle changed from 10 deg at around 12 s to avoid internal singularities, but it returned to 10 deg, and it was maintained at 10 deg to keep the maximum angular velocity around the x-axis. When escaping from the saturated singularities at around 28 s, the skew angle changed from 10 deg again for the AS-GSR, but it returned to 10 deg again around 35 s. On the other hand, the skew angle for the case of the AS-GSR+GL had a tendency to return towards the ordinary angle (54.73 deg) after leaving from 10 deg. This is because the AS-GSR+LG control law contains a null motion term based on the local gradient to keep the condition number of the ASCMGs equal to 1 as much as possible, and the condition number approaches 1 as the skew angle approaches the ordinary angle (54.73 deg). As the result of the perturbation of the skew angle in order to avoid internal singularities, the settling time resulting from the AS-GSR+LG became slightly longer than that of the AS-GSR for case 1. However, the returning of the skew angle to the ordinary angle at the end of maneuver is desirable, because the torque around an arbitrary axis other than the x-axis would be required at the next maneuver.

In case 2, at the beginning of maneuver, the skew angle was enlarged for the case of the AS-GSR, whereas it slightly shifted toward a smaller angle for the case of the AS-GSR+LG. Although there is such a large difference in the direction of the skew angle change at the beginning of the maneuver, in both the cases of the AS-GSR and the AS-GSR+LG, the skew angle reached the maximum limitation angle (80 deg) to extend the CMG angular momentum about the z-axis. Contrary to the results for case 1, after reaching 80 deg, the skew angle was maintained for a while, then shifted slightly towards a smaller angle in order to escape from the saturated singularity around 18 s, and then was maintained to such an angle for the case of the AS-GSR. On the other hand, for the case of the AS-GSR+LG, after the skew angle changed from 80 deg in order to avoid a saturated singularity, it became 80 deg again, and was maintained at 80 deg even after the end of maneuver. The skew angle began to return towards the ordinary angle after the end of maneuver for the AS-GSR+LG. This change in skew angle was induced by the null motion term for the ASCMGs. The gimbal angles returned to an angle of zero for the case of

the GSR and almost zero for the case of the AS-GSR, whereas at the end of maneuver, the gimbal angles δ_1 and δ_3 reached -90 deg for the AS-GSR+LG. The difference in the final gimbal angles did not always take place for maneuvers around the z-axis.

The results of the settling times for each of the steering control laws are summarized in Table 3. It is shown that the settling time for the AS-GSR and the settling time for the AS-GSR+LG were shorter than that of the GSR for the fixed-skew CMGs. This is because in the ASCMGs system the skew angle was changed from 54.73 deg to 10 deg for case 1 to extend the CMG angular momentum toward the x-axis, and the skew angle was changed toward 80 deg for case 2 to extend the CMG angular momentum towards the z-axis. This change in skew angle contributed to the acceleration of the angular velocity around the x-axis for case 1 and around the z-axis for case 2. In fact, for case 1, the maximum angular velocity around the x-axis was approximately 0.08 rad/s for the GSR, whereas it was approximately 0.11 rad/s for the AS-GSR and the AS-GSR+LG. Similarly, for case 2, the maximum angular velocity around the z-axis was approximately 0.12 rad/s for the GSR, whereas it was approximately 0.15 rad/s for the AS-GSR and the AS-GSR+LG. In Table 3, the reduction percentage of the settling time relative to the settling time for the GSR is also listed. As shown in Table 3, the AS-GSR and the AS-GSR+LG succeeded in a reduction of settling time, compared to the GSR for the fixed-skew CMGs, by approximately 5%.

These results show that the ASCMGs system is effective in reducing the settling time, compared to the CMGs with a fixed skew angle.

6. Conclusions

In contrast to the pyramid-type CMG systems that treat the skew angle as fixed, in this paper, the adaptive-skew pyramid-type CMGs (ASCMGs) was considered, in which the skew angle is treated as one of the controllable parameters. The mechanism for changing the skew angle among four CMG units was presented. The momentum envelopes and internal singularities were calculated according to the skew angles, and it was shown that the available maximum momentum around the z-axis or the x- and y-axes becomes large when the skew angle increases or decreases. In addition, the singular surfaces of the ASCMGs were analyzed and visualized from the viewpoints of the possibility of null motion using not only gimbals but also the skew angle. Referring to the existing steering laws for the fixed-skew

CMGs, the steering control laws for the ASCMGs were presented, and their effectiveness for fast attitude maneuvers was numerically studied, compared to the traditional CMGs with the fixed skew angle. The effectiveness of the ASCMGs will be experimentally validated using the experimental module, and other steering control laws that can more effectively utilize the degree of freedom associated with the skew angle will be proposed in the near future, taking into consideration the results of the singularity analyses presented in this paper.

Acknowledgment

This study was partially supported by a Grant-in-Aid for Scientific Research (C) (No. 22560783) from the Japan Society for the Promotion of Science and by the CASIO Science Promotion Foundation.

References

[1] G. Margulies, and J.N. Aubrun, Geometric theory of single-gimbal control moment gyro system, Journal of Astronautical Sciences, 26(1978) 159-191.

[2] B. Wie, Space vehicle dynamics and control, 2nd edition, AIAA Education Series, American Institute of Aeronautics and Astronautics, Inc. 2008.

[3] H. Kurokawa, A Geometric study of single gimbal control moment gyros -singularity problems and steering law, Tech. Rep. Report, Mechanical Engineering Laboratory, Japan, No.175, Jan., 1998.

[4] S. R. Vadali, H. S. Oh, and S. R. Walker, Preferred gimbal angles for single gimbal control moment gyros, Journal of Guidance, Control, and Dynamics, 13(1990) 1090-1095.
doi:10.2514/3.20583

[5] J. A. Paradiso, Global steering of single gimbaled control moment gyroscopes using a directed search, Journal of Guidance, Control and Dynamics, 15(1992) 1236-1244.
doi:10.2514/3.20974

[6] A. Fleming and I. M. Ross, Singularity-free optimal steering of control moment gyros, Advances in the Astronautical Sciences, 123-III (2006) 2681-2700.

[7] N. S. Bedrossian, J. Paradiso, E. V. Bergmann and D. Rowell, Steering law design for redundant single-gimbal control moment gyroscopes, Journal of Guidance, Control, and Dynamics, 13 (1990) 1083-1089.
doi:10.2514/3.20582

[8] V. Lappas and B. Wie, Robust CMG steering logic with gimbal angle constraints, AIAA Paper 06-6651, Aug., 2006.

[9] H. S. Oh and S. R. Vadali, Feedback control and steering laws for spacecraft using single gimbal control moment gyros, Journal of the Astronautical Sciences, 39(1991) 183-203.

[10] B. Wie, D. Bailey and C. J. Heiberg, Singularity robust steering logic for redundant single-gimbal control moment gyros, Journal of Guidance, Control, and Dynamics, 24(2001) 865-872.
doi:10.2514/2.4799

[11] B. Wie, Singularity escape/avoidance steering logic for control moment gyro systems, Journal of Guidance, Control, and Dynamics, 28(2005) 948-956.
doi:10.2514/1.10136

[12] K. A. Ford and C. D. Hall, Singular direction avoidance steering for control-moment gyros, Journal of Guidance, Control, and Dynamics, 23(2000) 648-656.
doi:10.2514/2.4610

[13] N. S. Bedrossian, J. Paradiso, E. V. Bergmann and D. Rowell, Redundant single gimbal control moment gyroscope singularity analysis, Journal of Guidance, Control, and Dynamics, 13(1990) 1096-1101.
doi:10.2514/3.20584

[14] H. Kurokawa, Constrained steering law of pyramid-type control moment gyros and ground tests, Journal of Guidance, Control, and Dynamics, 20(1997) 445-449.
doi:10.2514/2.4095

[15] H. Kurokawa, Exact singularity avoidance control of the pyramid type CMG system, AIAA Paper 94-3559, Aug., 1994.

[16] D. Jung and P. Tsiotras, An experimental comparison of CMG steering control laws, AIAA Paper 04-5294, Aug., 2004.

[17] J. Lee, H. Bang and H. Lee, Singularity avoidance by game theory for control moment gyros, AIAA Paper 05-5946, Aug., 2005.

[18] V. J. Lappas, S. Asghar, P. L. Palmer and D. Fertin, Combined singularity avoidance for redundant control moment gyro clusters, AIAA Paper 04-5131, Aug., 2004.

[19] S. Asghar, P. L. Palmer and M. Roberts, Exact steering law for pyramid-type four control moment gyro systems, AIAA Paper 06-6652, Aug., 2006.

[20] H. Kurokawa, Survey of theory and steering laws of single-gimbal control moment gyros, Journal of Guidance, Control and Dynamics, 30(2007) 1331-1340.
doi:10.214/1.27316

[21] A. F. Leve and G. N. Fitz-Coy, Hybrid steering logic for single-gimbal control moment gyroscopes, Journal of Guidance, Control, and Dynamics, 33(2010) 1202-1212.
doi: 10.2514/1.46853

[22] H. Schaub and J. L. Junkins, Singularity avoidance using null motion and variable-speed control moment gyros, Journal of Guidance Control, and Dynamics, 23(2000) 11-16.
doi: 10.2514/2.4514

[23] J. McMahon and H. Schaub, Simplified singularity avoidance using variable-speed control moment gyroscope null motion, Journal of Guidance, Control, and Dynamics, 32(2009) 1938-1943.
doi: 10.2514/1.45433

[24] H. Yoon and P. Tsiotras, Singularity analysis and avoidance of variable-speed control moment gyros, Journal of Guidance, Control, and Dynamics, 27(2004) 374-386.
doi: 10.2514/1.2946

[25] H. Yoon and P. Tsiotras, Spacecraft line-of-sight control using a single variable-speed control moment gyro, Journal of Guidance, Control, and Dynamics, 29(2006) 1295-1308.
doi: 10.2514/1.18777

[26] H. Yoon and P. Tsiotras, Spacecraft adaptive attitude and power tracking with variable speed control moment gyroscopes, Journal of Guidance, Control, and Dynamics, 25(2002) 1081-1090.
doi: 10.2514/2.4987

[27] K. Takada and H. Kojima, Receding horizon control on steering of control moment gyro for fast attitude maneuver, Transactions of the Japan Society for Aeronautical and Space Sciences, 52(2009) 1-10.
doi:10.2322/tjsass.52.1

[28] K. Takada, H. Kojima and N. Matsuda, Control moment gyro singularity-avoidance steering control based on singular-surface cost function, Journal of Guidance, Control, and Dynamics, 33(2010) 1442-1450.
doi:10.2514/1.48381

[29] H. Kojima, N. Matsuda, and K. Takada, Adaptive skewing pyramid-type CMGs for fast attitude maneuver, Transactions of the Japan Society for Aeronautical and Space Sciences, Space Technology Japan, 7(2009) 19-24.
doi:10.2322/tstj.7.19

[30] Y. Kanamura and H. Hanafusa, Inverse kinematic solutions with singularity robustness for robot manipulator control, Journal of Dynamics Systems, Measurement, and Control, 108(1986) 163-171.

[31] J. Crenshaw, 2-SPEED, a single-gimbal control moment gyro attitude control system, AIAA Paper 73-895, 1973.

[32] B. Wie, Singularity analysis and visualization for single-gimbal control moment gyro systems, Journal of Guidance, Control, and Dynamics, 27(2004) 271-282.
doi:10.2514/1.9167

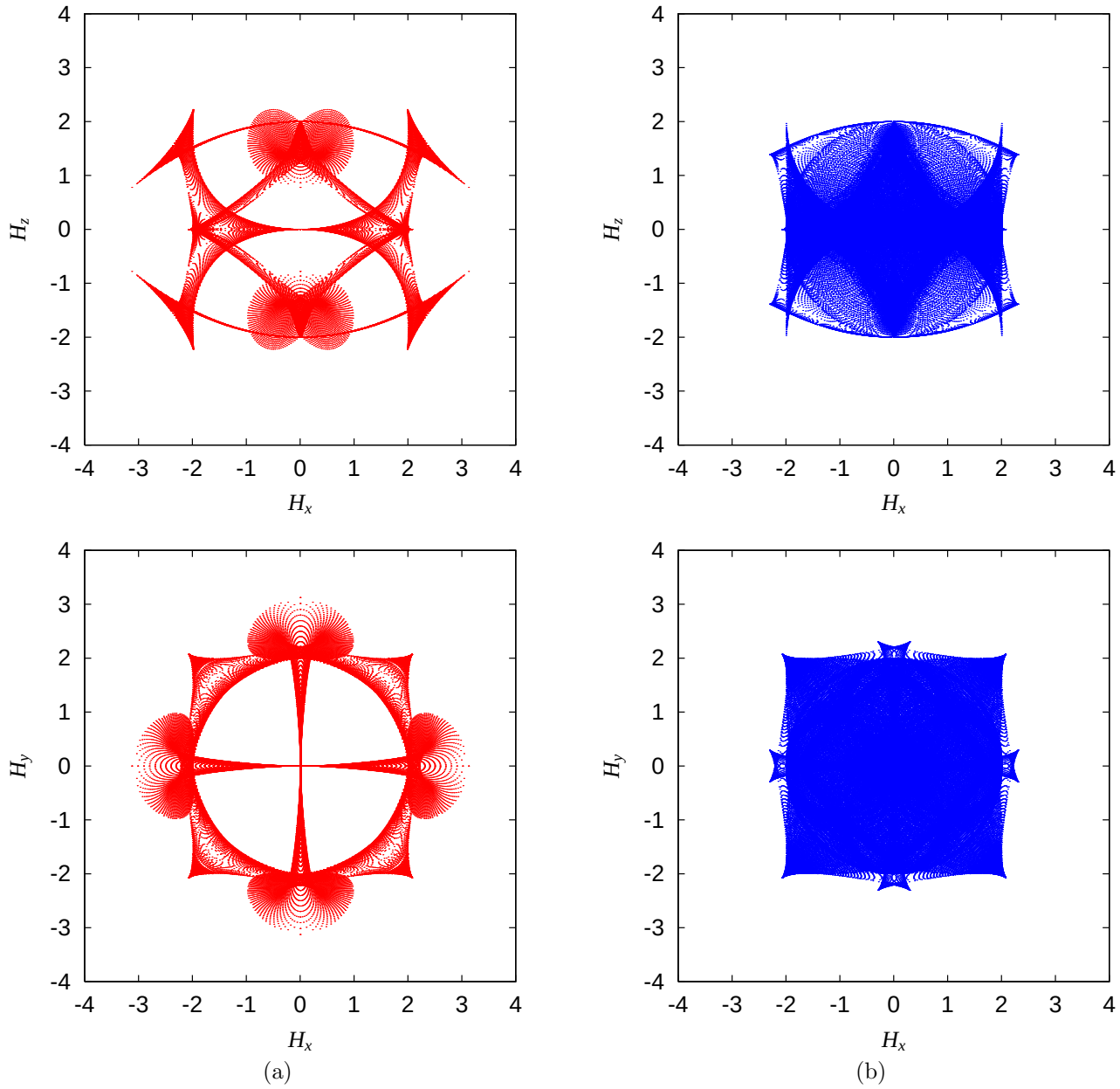

Figure 11: (a) Elliptic singularities and (b) hyperbolic singularities of ASCMGs.

Table 2: Simulation parameters.

Parameters	Value
$\boldsymbol{\delta}(0)$	[0, 0, 0 , 0] rad
$\dot{\boldsymbol{\delta}}(0)$	[0, 0, 0 , 0] rad/s
$\dot{\delta}_{\max}$	0.32 rad/s
$\beta(0)$	54.73 deg
$\beta_{\max}$	$4\pi/9$ rad (=80.0 deg)
$\beta_{\min}$	$\pi/18$ rad (= 10.0 deg)
$\dot{\beta}_{\max}$	0.32 rad/s
H	0.0419 Nms
$\boldsymbol{J}$	diag(1.5, 0.651, 1.11) kgm^2
k	5.0×10^{-6}
$\boldsymbol{K}_p$	0.09 $\boldsymbol{I}_3$ Nms
$\boldsymbol{K}_d$	0.4242 $\boldsymbol{I}_3$ Nms/(rad/s)
$\boldsymbol{W}$	diag(1, 1, 1, 1, 0.005)
$\tilde{\boldsymbol{W}}$	diag(1, 1, 1, 1, 1000)
$\lambda_0, \mu, \epsilon_0$	0.01, 10, 0.01
ω	0.5 rad/s
ϕ_i	$0, \pi/2, \pi$ rad
$\boldsymbol{q}(0)$	$(-1, 0, 0, 0)$ for case-1, $(0, 0, -1, 0)$ for case-2

Table 3: Comparison of settling times.

Steering control law	Settling time, s		Reduction rate average
	case-1	case-2	compared to GSR, %
GSR	75.12	49.90	-
AS-GSR	70.72	47.26	5.57
AS-GSR+LG	71.94	47.14	4.90

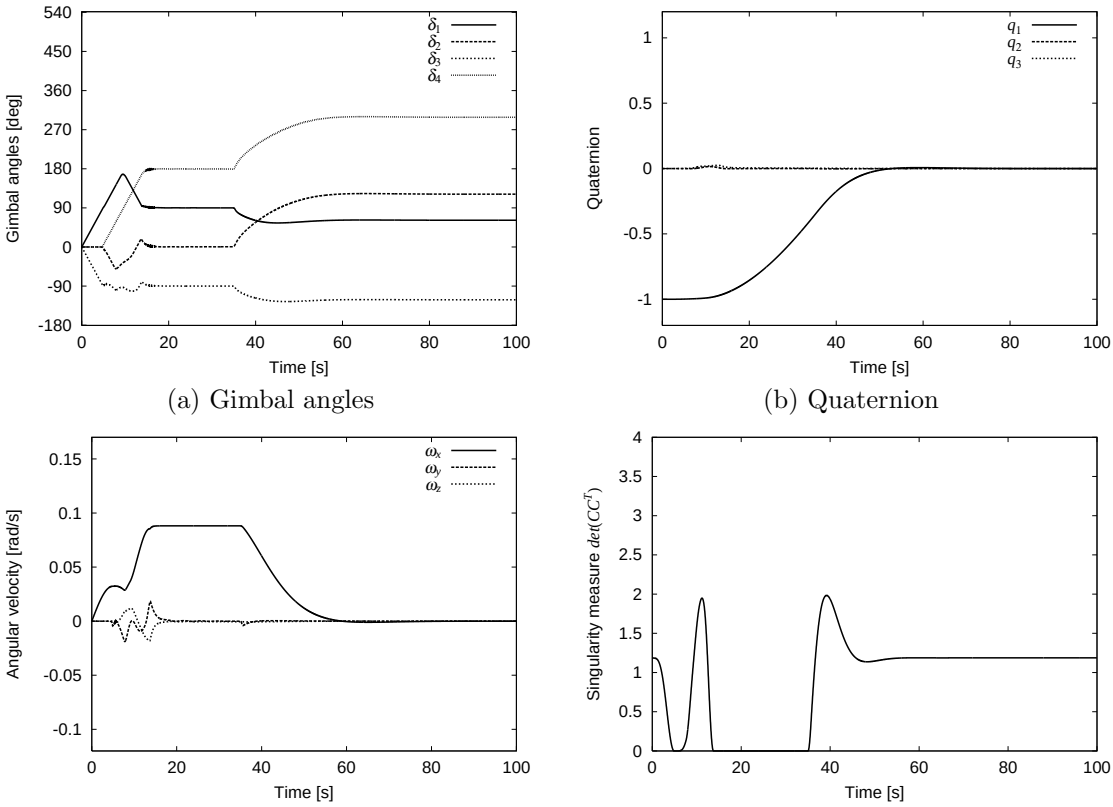

(a) Gimbal angles (b) Quaternion

(c) Angular velocity (d) Singularity measure

Figure 12: Results of the GSR for fixed-skew CMGs for case 1.

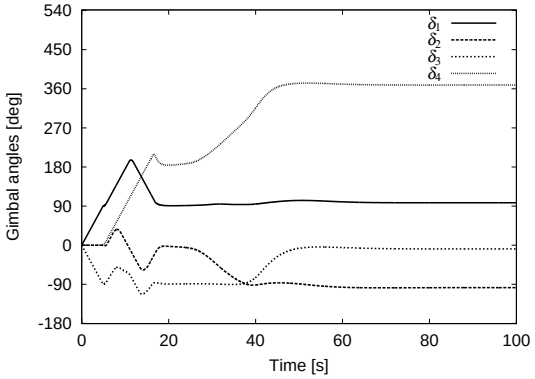

(a) Gimbal angles

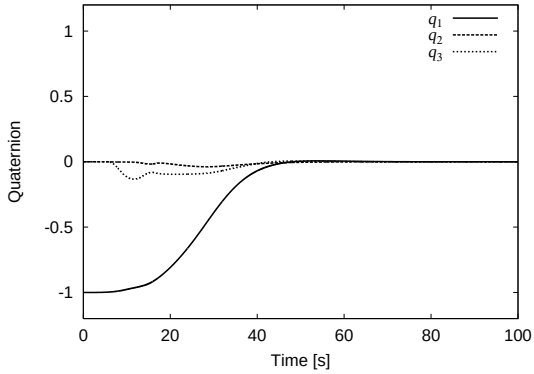

(b) Quaternion

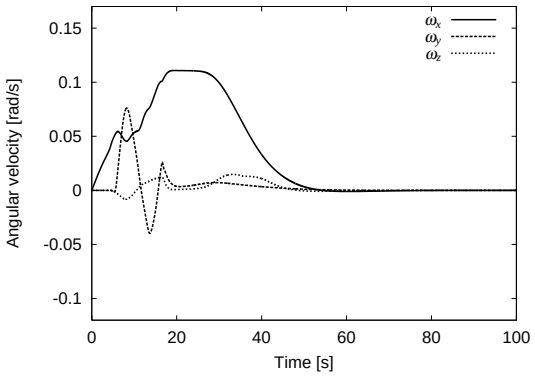

(c) Angular velocity

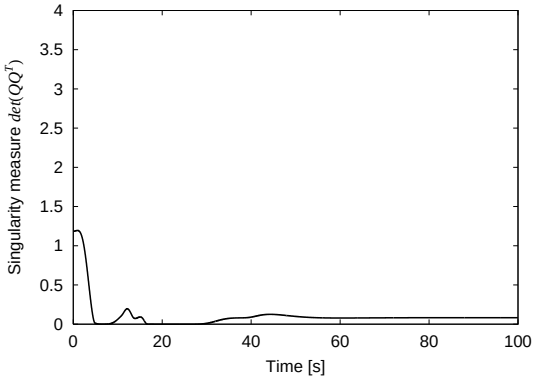

(d) Singularity measure

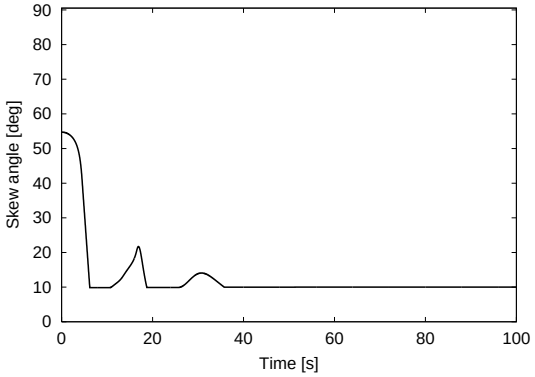

(e) Skew angle

Figure 13: Results of the AS-GSR for case 1.

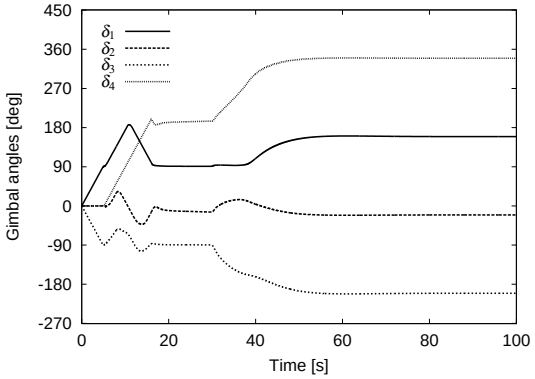

(a) Gimbal angles

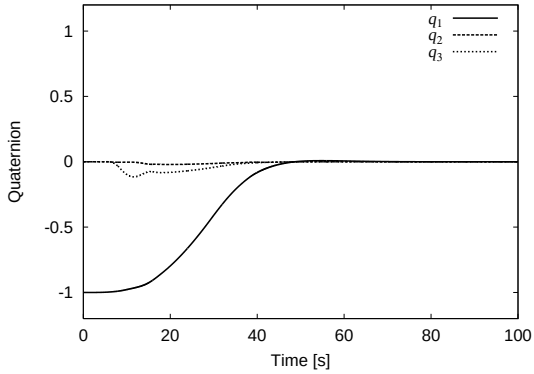

(b) Quaternion

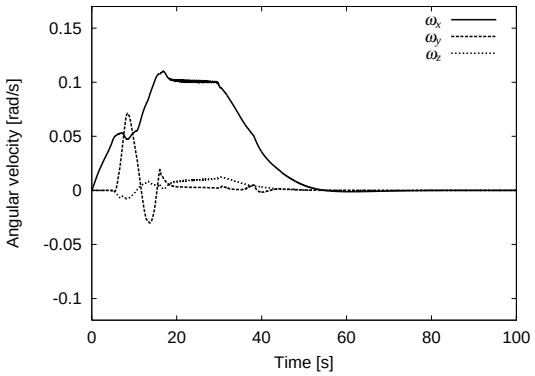

(c) Angular velocity

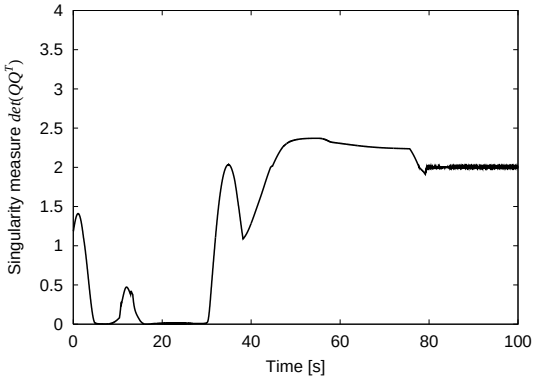

(d) Singularity measure

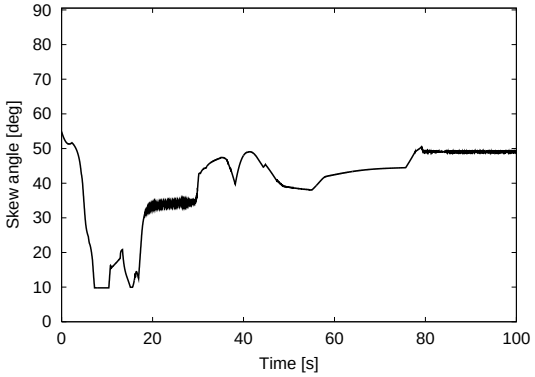

(e) Skew angle

Figure 14: Results of the AS-GSR+LG for case 1.

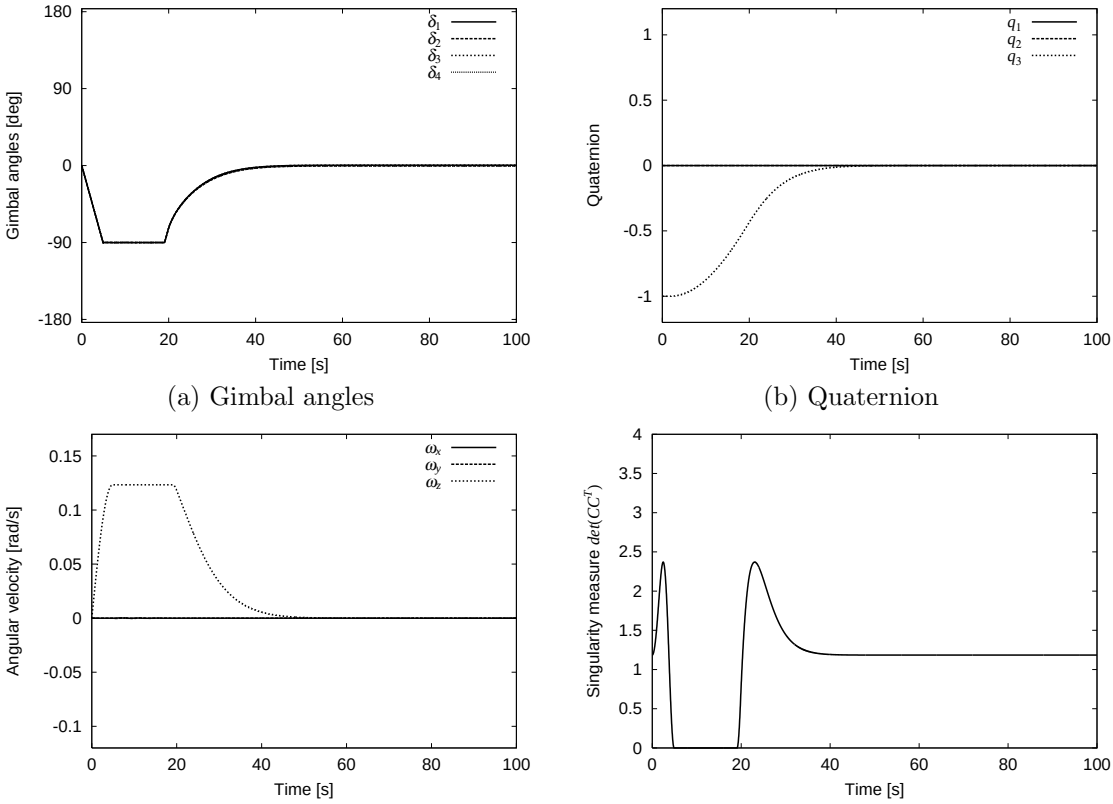

(a) Gimbal angles (b) Quaternion

(c) Angular velocity (d) Singularity measure

Figure 15: Results of the GSR for fixed-skew CMGs for case 2.

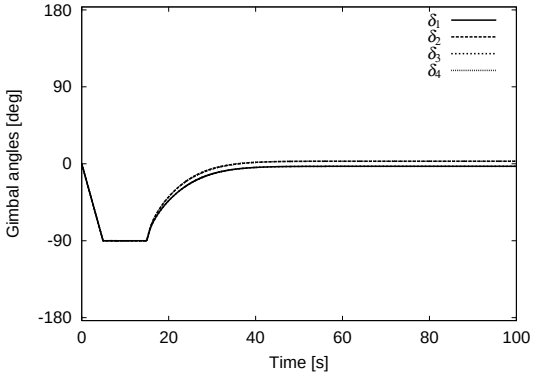

(a) Gimbal angles

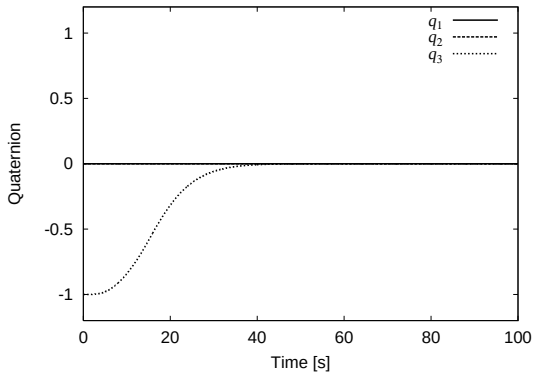

(b) Quaternion

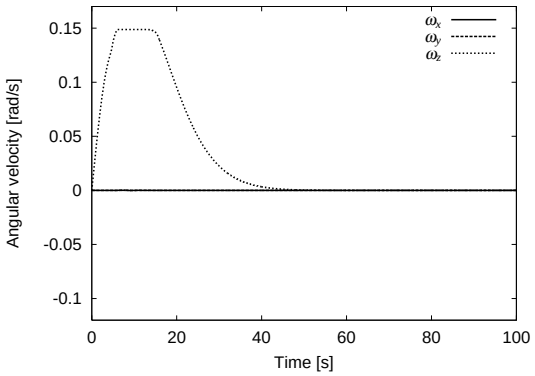

(c) Angular velocity

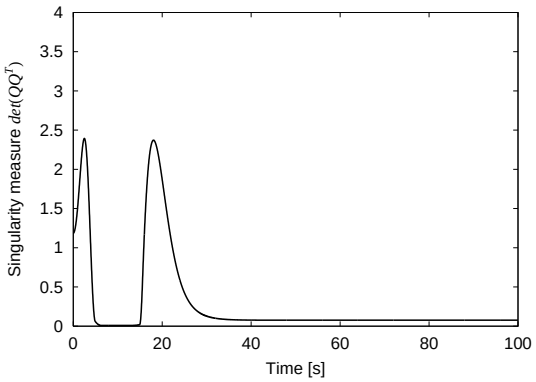

(d) Singularity measure

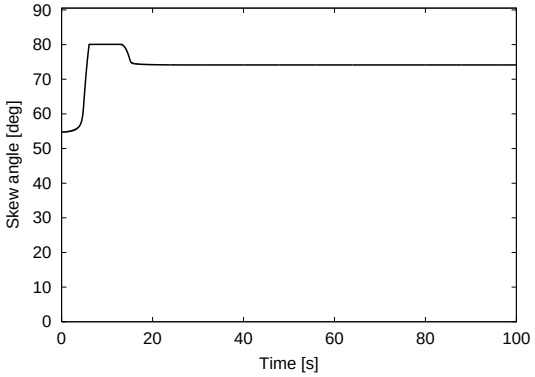

(e) Skew angle

Figure 16: Results of the AS-GSR for case 2.

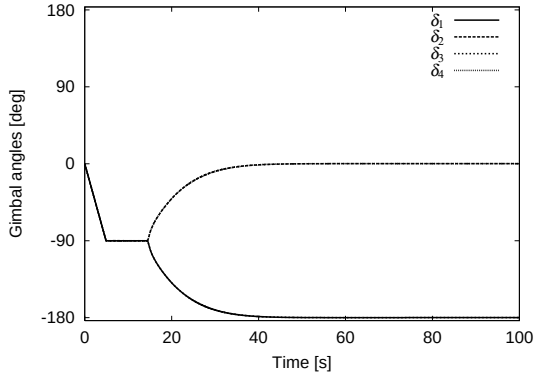

(a) Gimbal angles

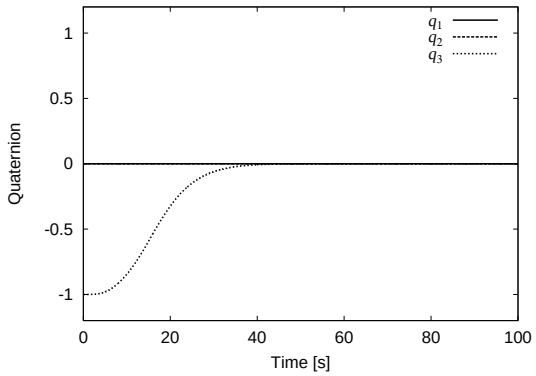

(b) Quaternion

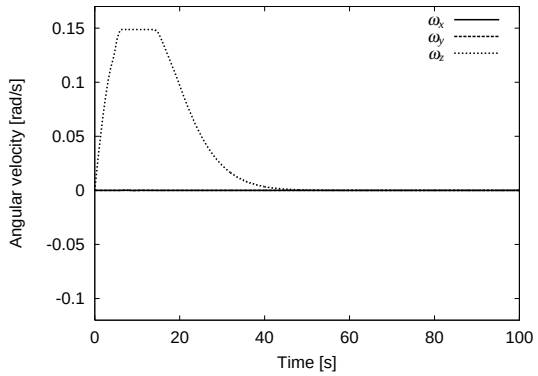

(c) Angular velocity

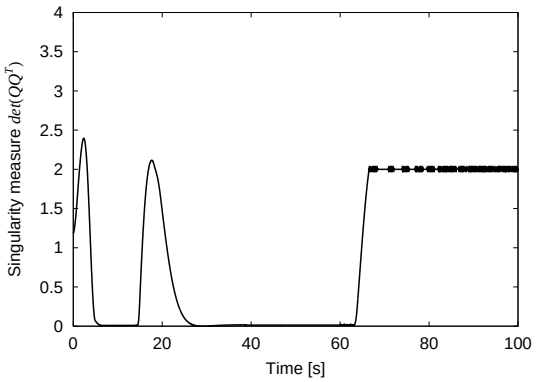

(d) Singularity measure

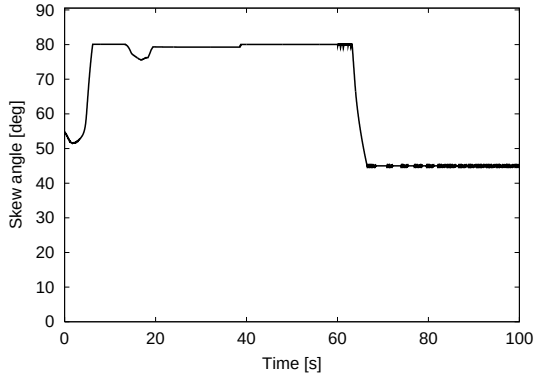

(e)Skew angle

Figure 17: Results of the AS-GSR+LG for case 2.